9-10-2015 12:00 AM

Investigation of flow and thermal behaviour in a pipe submerged in a hot fluid

Ben S. Steen, *The University of Western Ontario*

Supervisor: Dr. Kamran Siddiqui, *The University of Western Ontario*

A thesis submitted in partial fulfillment of the requirements for the Master of Engineering Science degree in Mechanical and Materials Engineering

Investigation of flow and thermal behaviour in a pipe submerged in a hot fluid

(Thesis format: Monograph)

by

Benjamin S Steen

Graduate Program in Engineering Science,
Department of Mechanical and Materials Engineering

A thesis submitted in partial fulfillment
of the requirements for the degree of
Master of Engineering Science

The School of Graduate and Postdoctoral Studies
The University of Western Ontario
London, Ontario, Canada

Abstract

Mixed convection through a pipe immersed in a hotter, stagnant fluid is used in HVAC systems, water heaters, chemical processes, etc. In this study, the effect of mixed convection on the flow and thermal structure of a fluid immersed inside a hotter, stagnant fluid was experimentally investigated. Temperature and velocity fields were obtained for a Reynolds number range of 330-6670, and a Grashof number range of 14000-95000 ($0.6 < Gr/Re2 < 0.0003$). It was found that the buoyancy-induced wall-normal velocity component altered the streamwise velocity structure and the temperature profiles. The mean streamwise velocity profile was skewed towards the bottom of the pipe for initially laminar flow only. A vertical temperature gradient was also observed in the internal fluid under these conditions, where the hotter fluid resided in the top region of the pipe. The Nusselt number was found to moderately follow the predictive Gnielinski correlation, with an additional dependence on the bottom wall temperature. This showed that an increase in the Grashof number tended to dampen the turbulent convective heat transfer. The influence of natural convection on the mean and turbulent velocity profiles was found to be almost negligible in the high Reynolds number range.

Keywords

Mixed convection; low Reynolds numbers; immersed pipe; near-isothermal fluid; temperature profile; particle image velocimetry (PIV); turbulence.

Acknowledgments

I would like to acknowledge the significant influence that my supervisor, Dr. Kamran Siddiqui, had on my educational development process throughout this study. His guidance, support, and deep understanding of the field was extremely valuable to my learning experience. I am very thankful for Dr. Kamran Siddiqui's expertise management. I wish to thank my parents and friends for their encouraging social support and motivation. I would also like to thank all my co-workers who helped with the experimental processes.

Table of Contents

List of Tables

List of Figures

List of Nomenclature

A	Pipe cross-sectional area, cm^2
c_P	Specific heat,
d	Diameter of seeding particles, μm
D_o	Outer pipe diameter, cm
D_i	Inner pipe diameter, cm
f	Friction factor
g	Acceleration due to gravity, cm/s^2
Gr	Grashof number
h	Convective heat transfer coefficient,
k	Thermal conductivity,
l	Integral length scale, cm
L	Length of the heat exchanger, m
L_D	Development length, m
$\dot{m}$	Mass flow rate, g/s
Nu	Nusselt number
Pr	Prandtl number
q	Heat transfer rate, W
q''	Heat flux, W/cm^2
R_{ij}	Cross correlation function

Re	Reynolds number
r_i	Inner pipe radius,
r_o	Outer pipe radius,
T	Controlled temperature, C
T_{inlet}	Inlet temperature,
T_{outlet}	Outlet temperature,
T_{inner}	Average circumferential inner pipe surface temperature, C
T_{outer}	Average circumferential outer pipe surface temperature, C
T_{bulk}	Bulk temperature, C
T_P	Characteristic response time, s
u	Instantaneous streamwise velocity profile, cm/s
u'	Streamwise turbulent velocity field, cm/s
u_*	Characteristic RMS velocity scale
U	Mean 2D velocity vector field, cm/s
$\overline{U}$	Mean streamwise velocity, cm/s
u_{RMS}	Streamwise root-mean-square velocity profile, cm/s
u_T	Terminal velocity, cm/s
v	Instantaneous vertical velocity profile, cm/s
v'	Vertical turbulent velocity field, cm/s
v_{RMS}	Vertical root-mean-square velocity profile, cm/s

y Vertical axis, cm

Greek Symbols

β Thermal expansion coefficient,

γ Specific gravity of seeding particles,

ϵ Turbulent energy dissipation rate,

ν Kinematic viscosity, cm^2/s

μ Dynamic viscosity,

ρ Density, g/cm^3

Θ Normalized temperature

τ_η Kolmogorov timescale, s

Chapter 1

1 Introduction

1.1 Convective heat transfer

Heat exchangers are vital to a wide variety of residential and industrial applications such as HVAC systems, chemical and petrochemical processes, food processing, automotive and aerospace sector, and power plants. A heat exchanger is mechanically designed to effectively transfer heat from one fluid medium to another via a separating solid conductor. The advantage of using fluids is their ability to increase the rate of heat transfer by the additional process of convection. The heat transfer rate between the two fluids is dependent on many factors, including the geometry of the heat exchanger, and the flow behaviour and thermal conditions of the two fluids.

The mode of convection present in the flow is dependent on the relative magnitudes of inertial and buoyant forces. Inertial or buoyant dominant flows indicate whether the given fluid is undergoing mainly forced convection or natural convection, respectively. The Reynolds number (Re) as defined in Equation (1.1) is a dimensionless quantity that can be used as a reference for forced convection in pipe flows [1].

$$Re = \frac{\rho \overline{U} D_i}{\mu} \quad (1.1)$$

In the above equation, the average fluid velocity in the pipe ($\overline{U}$) is the characteristic velocity scale, which is obtained by dividing the volumetric flow rate by the inner cross-sectional area of the pipe. The inner diameter of the pipe (D_i) is the characteristic length scale, ρ is the fluid density and μ is the dynamic velocity of the fluid.

The Reynolds number is the ratio between inertial and viscous forces acting on the fluid. When $Re \ll 1$, the fluids viscous forces prohibit a coherent inertial motion. When $Re \gg 1$, the inertial effects begin to increase but the viscous effects are still significant. In pipe flows, as the value of the Reynolds number exceeds 2000, the inertial forces become large enough to produce transitionally turbulent behaviour resulting in chaotic eddies.

Beyond a Reynolds number value of 4000, most fluids and geometries exhibit fully turbulent flow.

A dimensionless parameter that quantifies the strength of natural convection is the Grashof number (Gr) defined in Equation 1.2 [1].

$$Gr = \frac{g\beta\left(T_{surface} - T_{bulk}\right)D^3}{\nu^2} \qquad (1.2)$$

where g is the acceleration of gravity, β is the thermal expansion coefficient of the fluid, and ν is the fluid kinematic viscosity. The quantities $T_{surface}$ and T_{bulk} are the inner surface and bulk fluid temperatures, respectively. Grashof number expresses the ratio between the buoyant and viscous forces.

As mentioned above, the convective behaviour present in the fluids operating inside a heat exchanger increases the total heat transfer rate. Therefore, most heat exchanger systems typically utilize both forced and natural convection. When both natural and forced modes of convection are present in the heat exchanger, this is called mixed convection. The relative contribution of the inertial and buoyant forces can be quantified through a single ratio of Gr/Re^2 [2]. At a value of $Gr/Re^2 \ll 1$, the fluid exhibits very little natural convective behaviour in relation to the forced convection. At $Gr/Re^2 \gg 1$, the fluids buoyant forces are much more prevalent with relation to the inertial motion and hence, the natural convection mode dominates over forced convection. At a large enough value of Gr/Re^2, the buoyant forces can also induce turbulent behaviour, analogous to the turbulent threshold present in Reynolds number.

Mixed convection has a strong influence on the thermal and hydrodynamic structure present inside laminar flows [3]. Many studies have investigated the heat transfer rate during fully developed mixed convection through different geometries and experimental conditions including a large range of Re and Gr numbers. The onset of unstable stratification is strongly dependent on the Grashof number and/or the Reynolds number [4]. This buoyancy driven flow enhances the heat transfer rate. However, after the

convection induced mixing, reducing the temperature gradient, the bulk temperature of the fluid rises and the heat transfer rate can drop [5].

For a given geometry, the heat transfer rate of the system is positively correlated with the Re and Gr, i.e. increasing one of these increases the heat transfer rate of the system. On the contrary, the same heat exchanger with a fluid operating at a lower Re increases the local temperature of the output but not the heat transfer rate. Extensive research has been conducted in the past to study forced convection in pipe flows, which occurs primarily at high Reynolds numbers. However, very limited research work has been performed for pipe flows at low Reynolds numbers. Although a wide range of heat exchanger applications involve high Reynolds numbers and hence forced convection. There are growing applications where the heat exchange occurs at low Reynolds numbers. Applications operating at low Re are becoming more popular in the green energy industry. Such type of flow are also present in chemical vapour deposition (CVD), biomedical applications and in the food process industry.

In a large number of heat exchanger applications, both fluids are in motion and hence, either forced or mixed convection modes exists in each fluid. Heat exchangers where one fluid is in motion while the other is stagnant are relatively few but such heat exchangers have numerous applications in food process industry, and chemical and nuclear reactors. The primary function of the heat exchanger in these applications is to add or remove heat from the stagnant fluid medium via the fluid flowing through the piping system immersed in the stagnant fluid.

The thermo-fluid process inside the immersed pipe is expected to be different from other types of heat exchanger applications. Being immersed in a larger stagnant fluid domain, the pipe is exposed to an almost isothermal condition of the stagnant fluid. Hence, the fluid dynamics inside the pipe is expected to influence the thermal boundary conditions at the pipe wall or vice versa. Furthermore, the mode of convection heat transfer is also expected to play a role in the heat exchange between the pipe fluid and the surrounding stagnant fluid. There is however a scarcity of studies investigating the thermo-fluid

process inside the pipe immersed in a stagnant isothermal fluid. This particular problem was the focus of this thesis.

The specific geometry of interest in this study is a fluid undergoing convection (forced and mixed) through a pipe that is immersed in a hotter stagnant fluid maintained at a uniform bulk temperature. To the best knowledge of the author, no thermo-fluid investigation has been conducted on such a geometry.

1.2 Heat transfer for fluids flowing in a channel

Due to the scarcity of previous studies on the thermo-fluid behavior in a submerged pipe flow, the literature review is primarily comprised of previous studies investigating thermo-fluid process in channel flows subjected to wall heating in the presence of mixed convection heat transfer. There are several studies that investigated bulk properties of a fluid forced through a channel with bottom heating. For example, Mahaney et al. [3] and Maughan and Incropera [6] investigated the longitudinal change in Nusselt number (Nu) and coefficient of friction along the heating section of a thermofluid circuit. They both observed an increase in the Nusselt number along the channel. This enhancement was attributed to the increase in natural convection along the channel, which increased the convective heat transfer rate by disrupting the thermal boundary layer. In these studies, the Nusselt number at the entrance region was minimal because the mode of convection was mainly forced, and natural convection was not developed. They also found that an increase in Gr accelerates the onset of convective flow, while an increase in Re decelerates this onset.

Osborne and Incropera [4&7] investigated mixed convection through a square channel with bottom and top heating during laminar and turbulent flow. Their main objective was to quantify the local Nusselt number near both the top and bottom wall regions of the channel. Forced convection was found to be prevalent at the top of the channel, while natural convection dominated at the bottom, increasing the Nusselt number. During laminar flow, the top region exhibited a thermal boundary layer in which rising plumes

from the bottom wall could not penetrate. Patil and Babu [8] investigated the convective heat transfer in a square duct with uniform thermal boundary conditions. They concluded that the average Nusselt number throughout the duct was positively correlated with the Gr/Re^2 and Prandtl number (Pr) values. The correlation was stronger at a lower Reynolds number, i.e. at lower Re, the increase in Gr/Re^2 or Pr resulted in a larger increase in the Nusselt number.

An experimental investigation of the region immediately adjacent to the bottom heating wall of a square channel during forced convection was conducted by Gajusingh and Siddiqui [9]. They researched the effect of heat transfer on the near wall region for originally laminar and turbulent flows. It was concluded that high buoyancy driven flows generated turbulence in originally laminar flow with large Gr. In the case of originally turbulent flow, the buoyant forces in the near wall region dampened local turbulent fluctuations. They quantified the instability of the fluid in this region due to stratification with the Richardson (Ri) number. They argued that the unstable stratification generated by bottom heating enhanced turbulence in originally laminar flows, but decreases its magnitude in originally turbulent flows.

Nicholl [10] investigated the effects of bottom heating on the turbulent boundary layer for unstable and stable stratification of air in a wind tunnel. The difference between the bulk and wall temperatures ranged from 20 to 100 C. It was found that during unstable stratification, the mean velocity and turbulent velocity magnitudes at the heated surface near the inlet of the heater were larger in magnitude with respect to the velocities further downstream of the heater. It was concluded that the turbulent boundary layer experienced a damping effect due to the present convective boundary layer. Similarly, Arya [11] experimentally investigated the effects of mixed convection on the mean and turbulent velocity profiles in a fully developed turbulent flow over a bottom flat plate for both stable and unstable stratification. It was found that the convective heat transfer coefficient and the coefficient of friction decreased with an increase in thermal stability, where the viscous sublayer grew in thickness with increasing stability. For turbulent flows during stable stratification, it was found that turbulence was damped with an increase in stability.

Rued et al. [12] experimentally and numerically investigated mixed convection in a square channel with a single heated side wall. They focused on researching the effects of wall intersections on the flow and thermal structures. An increase in the Nusselt number was observed in the corner region of wall intersection. This convective heat transfer enhancement was evidently attributed to the asymmetry of the corner region, and was also found to decrease with an increase in distance from the heated surface. Fukui and Nakajima [13] investigated the effect of bottom heating and unstable stratification generation in the near wall region for fully developed turbulent flow between two horizontal plates. They found an increase in the streamwise velocity fluctuations and a decrease in wall-normal velocity fluctuations with an increase in the Richardson number.

Hirota et al. [14] experimentally investigated the flow and thermal structures present during mixed convection in a bottom heated square duct for fully developed turbulent flow. Their focus was on the flow structure in a plane residing normal to the direction of flow. They found that in the center region of the duct, the eddy diffusivity of the fluid was higher for the heated cases than for the unheated cases. The comparative eddy diffusivity then became comparable at the near wall regions symmetrically. They also concluded that the buoyantly induced currents had a larger influence on the momentum transport with respect to the heat transport. Yamada and Ichimiya [15] numerically investigated mixed convection inside a square duct for both insulated walls, and uniform temperature wall conditions. They focused on the velocity field normal to the direction of flow, similar to Hirota et al. [14]. They found that the buoyant forces present under uniform wall temperature conditions influenced the development of convective currents with an increase in downstream distance.

1.3 Flow visualization

Some studies focused on visualizing the flow behaviour of thermofluids in order to conceptualize and quantify the mixed convection. For example, Rued et al. [12] used laser Doppler anemometry to study the flow structures in a duct with a side heated wall, as mentioned above. Perry and Hoffman [16] used X-wire probes to investigate the

velocity of fluid over a horizontal heated plate. They discovered that the fluctuating velocity fields were most prominently due to spurious pressure gradients than due to the mean flow motion. Wang et al. [17] investigated flow patterns in a bottom heated square channel using a shadowgraph technique. In their experiment, the Reynolds number ranged from 100 to 1000 and the Grashof number ranged from 2.8×10^6 to 2.5×10^7. They identified four distinct flow patterns between these experimental ranges: laminar forced convection, laminar mixed convection, transient mixed convection, and turbulent free convection. Lin and Lin [18] experimentally investigated mixed convection for air through a bottom heated rectangular channel using a smoke tracer. The range of Reynolds number was from 9 to 186, and the Grashof number was up to 5×10^6. They concluded that an increase in the Grashof number and/or a decrease in the Reynolds number changed the flow structure from periodic to quasiperiodic. Chaotic flow structures were even observed in some cases.

Mixed convection in different geometries were experimentally investigated by Nandakumar et al. [19] for a Grashof number up to 5×10^5. They found that either two or four longitudinal vortices occurred depending on the aspect ratio of the channel and the Grashof number. A numerical investigation of laminar mixed convection in a bottom heated square duct was conducted by Huang and Lin [20]. They focused on studying the flow behaviour under different Gr/Re^2 ratios. They concluded that an increase in the buoyancy-inertia ratio Gr/Re^2, the flow structure altered from a steady vortex into chaotic flow. This occurred typically at $Gr/Re^2 = 25$. Sookdeo and Siddiqui [21] investigated the mixed convection flow structure in a pipe utilizing particle image velocimetry (PIV) technique. They used a Reynolds number range of 150 to 900 with four different heating conditions and an unheated condition. To eliminate the distortion made by the curved surface, a square case filled with the same fluid was place around the tube in a small measurement section as a corrective measure for the image distortion due to pipe's curvature. They found that the collector heating had a significant effect on the mean velocity, inducing a vertically asymmetrical velocity profile over the range of Reynolds numbers and heating conditions. They also observed a stably stratified layer in the upper regions of the pipe and unstable stratification in the bottom regions.

Elatar and Siddiqui [22, 23] experimentally investigated mixed convection in a channel subjected to heating through bottom at low Reynolds numbers ($750 \geq Re \geq 150$), and large Grashof numbers resulting in buoyancy-inertia ratios ranging from 9 to 206. They imaged the internal flow structures non-invasively by employing the PIV technique. They were able to measure fluid velocity in a plane parallel to the flow direction and normal to the bottom wall. They also acquired velocity measurements in two planes parallel to the bottom wall at different heights in the near wall region. They found that the dominant natural convective currents induced chaotic turbulent behaviour in the fluid during initially laminar flow conditions. They also concluded that a coherent reverse current occurred in the top, cooler region of the pipe for $Gr/Re^2 > 55$, which increased in magnitude with an increase in this ratio.

1.4 Objectives

It was shown in the previous sections that several studies have been conducted on mixed convection in square and circular channels (pipes) under initially laminar and turbulent flow conditions. However, to the knowledge of the author, no studies have been conducted on the quantitative effect of mixed convection on the flow and thermal behaviour inside a pipe submerged in an isothermal fluid, despite its use in several applications. Therefore the present research is aimed at improving the knowledge and core understanding of the heat transfer mechanisms present inside such a geometry. The objectives of this study are as follows,

1. To quantify and investigate the mean and turbulent velocity structures present inside the pipe.
2. To quantify and investigate the internal temperature field in order to understand the heat transfer mechanisms present.
3. To explore the underlying effect of mixed convection on these structures

1.5 Thesis layout

The first chapter introduces the topic, discusses the heat exchange process involving fluids and the need for present investigation of thermo-fluid behavior in the specific geometry considered in this research. A brief literature review of studies focused on the fundamental heat transfer process to a fluid from heated wall is also presented. The chapter concludes with the objectives of the present dissertation. The second chapter focuses on the experimental setup and measurements. It provides details of the experimental apparatus used in this study along with instrumentation and measurement technique deployed to conduct the detailed investigation of the underlying thermo-fluid processes. The third chapter presents the detailed fluid temperature structure inside the submerged pipe obtained from thermocouple measurements. The variations in the local fluid temperature are presented and discussed in the context of the heat exchange process. The heat transfer rate and other critical dimensionless parameters also presented and their trends are discussed. The fourth chapter provides a detailed flow behaviour inside the pipe over a range of conditions obtained from PIV measurements. The variations in the mean and turbulent flow structures and their impact of the heat transport process are also discussed. The fifth chapter combines the key conclusions from earlier chapters and presents the main conclusions from the present study along with some recommendations for the future extension of the current work.

Chapter 2

2 Experimental Conditions

Experiments were conducted in a laboratory environment in a specially built test heat exchanger.

2.1 Experimental Apparatus

The test heat exchanger was comprised of a rectangular reservoir for the higher temperature fluid hereinafter referred to as the secondary (hot) fluid. The reservoir was made of 0.63 cm thick glass plates as the reservoir walls. The bottom was also made of 0.63 cm thick aluminum plate (see Figure 2.1a). The top of the reservoir was left open, exposed to the room pressure and temperature, which was approximately constant throughout the experiments. Heating of the reservoir fluid was achieved through the bottom aluminum plate. The aluminum plate was heated by a radiant heater, which was placed 8 mm below the aluminum surface, facing upward. This allowed the aluminum plate to be uniformly heated. During a given experimental run, the non-uniform temperature of the aluminum plate was kept constant using a PID controller (ZESTA-ZCP513). A K-type thermocouple located near the measurement location was used as a feedback for the temperature control. A glass tube of 2.54 cm (1 inch) internal diameter (0.32 cm or 1/8th inch wall thickness) and 1 m long was inserted through the center of the side walls of the reservoir such that the glass tube was fully submerged in the reservoir fluid, as shown in Figure 2.1(a). The red box in this figure illustrates the region in which PIV and temperature measurement were made. A cooler fluid, hereinafter referred to as the primary (cold) fluid passed through the tube and heat transfer occurred from the reservoirs hot fluid to the primary fluid. This heat transfer is referred to as the primary heat transfer.

Water was used as the primary and secondary fluids. The primary fluid was flowing in a closed circuit as illustrated in Figure 2.1(b). The primary fluid was drawn from a 10-litre reservoir tank and circulated through the loop by a pump (Little Giant, 2E 38N). Due to the heat transfer to the primary fluid in the test heat exchanger, its temperature increased

at the heat exchanger exit. To maintain similar inlet conditions, the heat gained by the primary fluid was removed via a secondary heat exchanger. The secondary heat exchange occurred in a 50-gallon tank. The primary fluid was passed through a copper coil submerged in 50 gallons of tap water at room temperature. A magnetic driven pump was used to stir this reservoir tank to enhance heat transfer. Preliminary test results showed that for a given run, the 50-litres of water had enough capacity to remove the heat added to the primary fluid in the primary heat exchange process and hence, to maintain the same conditions for the primary fluid at the inlet of the heat exchanger test section. The primary fluid exiting the secondary heat exchanger, then entered a 10-litre storage tank. A ball-valve downstream of the pump was used to control the volumetric flow rate of the primary fluid, which was measured by a flow meter (0 to 1 gpm ± 2%) located downstream of the valve (see Figure 2.1b). The primary fluid temperature at the inlet of the test heat exchanger was maintained at 21 ^{o}C.

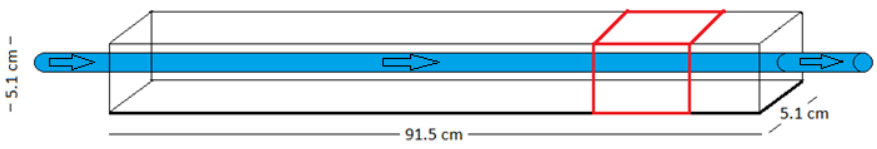

A.

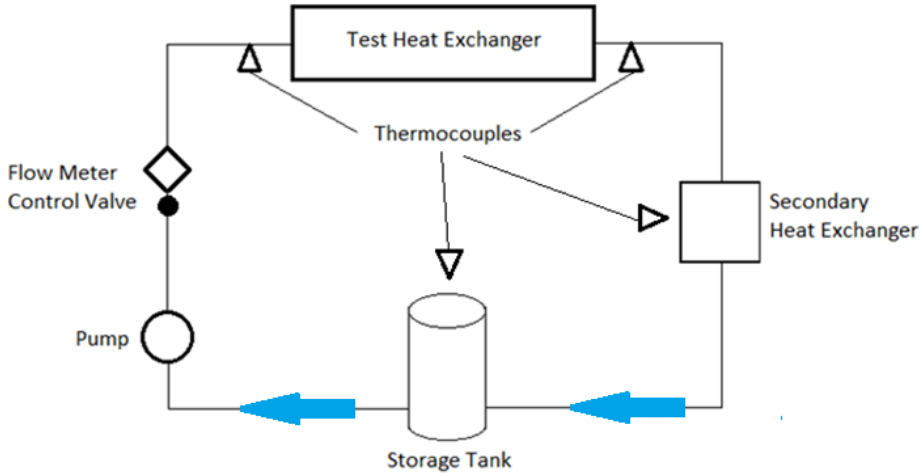

B.

Figure 2.1: A) Test heat exchanger illustration and dimensions, B) Idealized fluid circuit use in experimentation

The test heat exchanger and the radiant heater were supported by a rectangular wooden frame with a height of 1.2 m, width of 0.42 m, and length of 1.15 m (see Figure 2.2). The test heat exchanger and radiant heater both rested on adjustable shelves attached to the sides of the wooden frame. The height of the center of the glass channel was 0.55 meters off the ground.

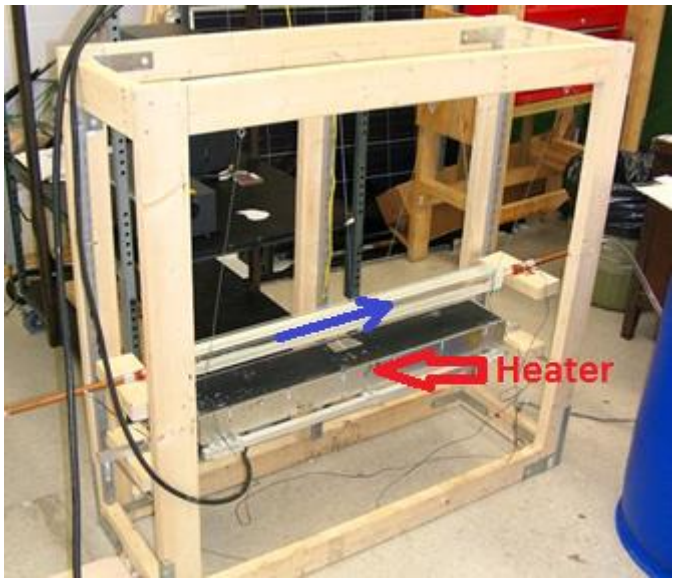

Figure 2.2: Experimental Facility used for experimentation

The upstream side of the glass tube in the test heat exchanger was connected to a straight copper pipe (0.5 inch ID) of 1 m in length. The purpose of this copper pipe was to allow the fluid to enter the test heat exchanger in a fully developed state. The upstream end of the copper tube was connected to the pump via a plastic hose. Two equations were used to compute the maximal development length; one for the laminar flow and the other for the turbulent flow, given as follows [24],

$$L_D = 0.06\, D_i\, Re \quad Laminar$$

$$L_D = 1.6\, D_i\, Re^{0.25} \quad Turbulent$$

where, L_D is the flow development length, D_i is the inner pipe diameter and Re is the Reynolds number of the flow based on the pipe diameter. To ensure that the flow was fully developed for the given flow rate range, the development length was computed for the highest Reynolds numbers in both the laminar and turbulent regimes considered in this study. The results showed that the length of the copper tube was sufficient enough to provide fully developed flow at the entrance of the test heat exchanger.

Five mass flow rates were considered in this study which were 0.0031, 0.0062, 0.0125, 0.0378, and 0.6356 kg/s. The corresponding Reynolds numbers at room temperature were

330, 660, 1330, 4000 and 6670, respectively. For each flow rate, five different bottom wall temperatures of 30, 40, 50, 60 and 70°C were considered. To ensure steady state conditions were attained before testing, there was a 20 minute waiting period between tests.

The chosen Reynolds numbers were intended to cover relatively low flow rates through the transition into turbulence and onwards. With these flow rates, there existed a threshold temperature in which bubbles began to generate in the reservoir fluid, which obstructed imaging of the submerged channel flow. To avoid this issue a criterion was set based on the condition that after waiting 20 minutes for the system to reach a steady state after changing the experimental conditions, there must have been at least five minutes of moderately bubble-free image acquisition. Due to this criterion, the experimental conditions utilized for the flow rates used for PIV experimentation excluded the highest temperature condition of 70°C, as well as the lowest flow rate condition of $Re = 330$.

2.2 Experimental Measurements

Temperatures were recorded at several locations inside a cross section of the test heat exchanger using T-type thermocouples (uncertainty of ± 0.5 C). These thermocouples were grouped into two sets; one set of thermocouples to measure the temperature outside the glass channel, while the second set of thermocouples measured the fluid temperature inside the glass channel. In the first set, three thermocouples were attached to the outer surface of the glass tube to measure the wall temperature of the glass tube (see Figure 2.3a). Another thermocouple was attached to the bottom aluminum plate to measure its temperature.

To measure the fluid temperature inside the tube cross-sectional plane with high spatial resolution, a rake was built from aluminum wire to support nine thermocouples in the cross-sectional plane as shown in Figure 2.3(b). The rake was inserted from the downstream end of the glass tube and was supported by a long thin aluminum tube to maintain axial alignment. The 90 degree elbow in the downstream copper tube held the

aluminum tube in place. The thermocouples were fed through the center of this aluminum tube into the front of the rake. The rake was positioned 20 cm from the downstream end of the test heat exchanger. Two additional thermocouples were used to measure the temperature of the primary fluid at the inlet and outlet of the test heat exchanger.

A National Instruments data acquisition system comprised of two DAQ cards (NI 9211) and a chassis (NI cDAQ-9174) was used to acquire data from these thermocouples. The data acquisition system was connect to a PC and LabView was then used as the data acquisition software. As mentioned earlier, the data acquisition began once the system reached a steady state. This was monitored in real-time through the temperature graph present in LabView. The temperature data graph of temperature vs. time visually indicated when a steady state was reached. The data then recorded at a sampling rate of 3 Hz (based on the response time of thermocouples) for approximately five minutes for each experimental condition. The average temperature values were obtained by time-averaging the corresponding temperature data for each thermocouple.

Generally, the resistance of a thermocouple is dependent on the soldered connection of the two metals at its tip. Different thermocouples will then result in different voltage readings for the same temperature. Each thermocouple must therefore be individually linearly calibrated in order to offset any bias error present. The calibration was conducted using a 500 mL glass insulated beaker. A mercury-bulb thermometer was used as the reference. The calibration was conducted at six temperature set points (9, 19, 26, 31.5, 38 and 45.5 °C) by varying the temperature of the liquid bath. These temperatures cover the temperature range of the experimental conditions. The calibration equations for each thermocouple were obtained through linear regression between the measured and reference temperature values. These calibration equations were then used to correct the temperature data obtained during actual experiments.

A.

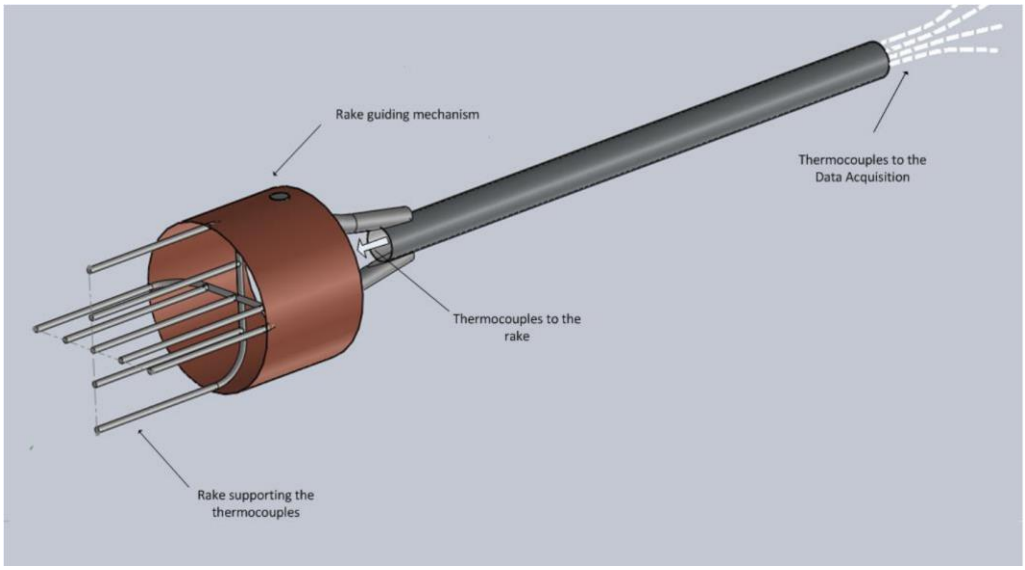

B.

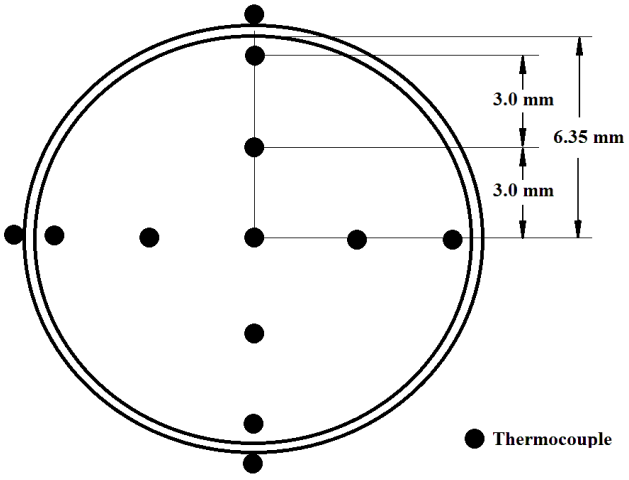

Figure 2.3: A) Constructed thermocouple rake inserted inside the pipe to acquire the internal temperature field measurements, B) the cross sectional arrangement of each thermocouple with respect to the pipe.

2.3 Particle image velocimetry

Particle image velocimetry (PIV) was employed to measure the two-dimensional velocity field of the primary fluid in the vertical mid-plane of the glass pipe. The PIV system is displayed in Figure 2.4. The primary fluid was initially seeded with glass particles of 15 μm diameter. A 120 mJ Nd:YAG laser (SoloPIV 120XT 532nm) was used to illuminate

these reflective seeding particles present in the measurement plane. A CCD camera (VA-4M32, Vieoworks) with a resolution of 2336x1752 pixels was used to capture images of the reflected laser light. A CORE-DVR image acquisition system (IO Industries) was used to acquire and store images. The CORE-DVR was connected to a PC and controlled by the Coreview software. A four-channel pulse generator (555-4C, Berkley Nucleonics Corporation) was used to time and coordinate the laser pulses and synchronize them with the camera.

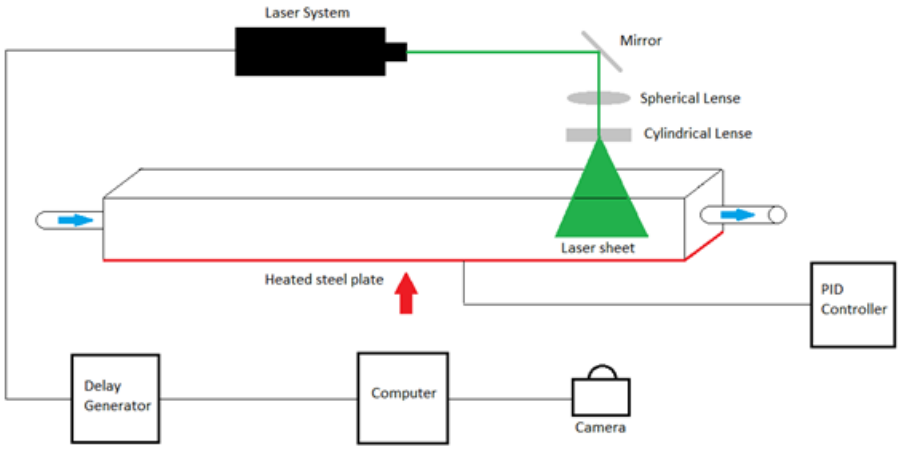

Figure 2.4: Idealized Particle Image Velocimetry (PIV) setup

To ensure a uniform distribution of the seed particles, they were rigorously stirred in a 200 mL beaker. This solution was then poured into the ten liter reservoir and mixed thoroughly with the working fluid. For the seeding particles to accurately follow the fluid flow, they must have been neutrally buoyant in the fluid. The specific gravity of the seed particles was approximately 2.5. Hence, to confirm that they accurately followed the flow, the response time of the particles was computed, i.e. how quickly the particles responded to any change in the flow behavior. The characteristic response time of the seed particles can be computed using the following equation,

$$T_P = \frac{u_T}{g} \quad (2.1)$$

where T_P is the particle response time, u_T is the particle terminal velocity and g is the acceleration due to gravity [25]. The terminal velocity can be computed using the following equation,

$$u_T = \frac{(\gamma - 1)d^2 g}{18\nu} \quad (2.2)$$

where γ and d are the specific gravity and diameter of the seed particles, respectively, and ν is the kinematic viscosity of water [26]. For the seed particles used in the present study, the response time was found to be $18.75\ \mu s$. The smallest timescale expected in the flow is the Kolmogorov timescale (τ_η) which is given by,

$$\tau_\eta = \left(\frac{\nu}{\epsilon}\right)^{\frac{1}{2}} \quad (2.3)$$

Where, ν is the kinematic viscosity and ϵ is the energy dissipation rate [27]. The dissipation rate can be approximated as,

$$\epsilon \sim \frac{u'^3}{l} \quad (2.4)$$

Where, u' is the streamwise turbulent velocity and l is the integral length scale [28]. For the turbulent flow regime in the present study, the Kolmogorov time scale was computed to be approximately 1 s, which was more than 10^5 times larger than the response time of the seed particles and hence, it confirms that the particles accurately followed the flow [25, 29, 30].

The laser light emitted from the laser head was a collimated cylindrical beam. A set of optics was used to transform it into a light sheet and align it with the measurement plane. For this purpose, the laser beam first passed through a spherical lens and then spread out into a two dimensional sheet by passing through a cylindrical lens. An apparatus attached to the facility directly above the test heat exchanger mirrored the laser sheet 90 degrees downwards to illuminate the measurement plane in the center of the glass pipe. The camera was centered on a region 80 cm downstream of the test heat exchanger entrance.

The cameras field of view was 3.5 cm × 1.4 cm. Note that the center of this measurement region coincided with the location of temperature measurements using the thermocouple rake.

The measurement plane for PIV imaging was inside the circular glass tube. The tubes curved surface would distort the images as acquired by the camera located outside (see Figure 2.5a). This is due to the reason that the camera receives light at different incident angles due to the curved surface and a change in density of the internal water and external air mediums. The experimental setup described above allows for a correction in the distortion made by this curved surface. As shown in Figure 2.5(b), the light does not refract at the surface of the glass tube because the internal and external mediums are the same. There is also no refraction angle when the light passes from water to air because it exits the square channel normal to its surface. The minimal refraction due to the thickness of the glass pipe was considered negligible due to its thinness [31].

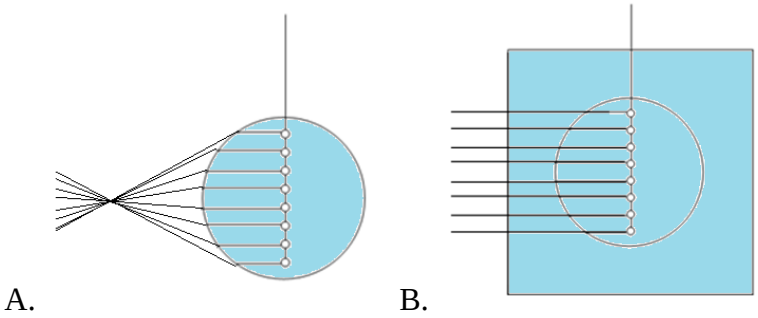

Figure 2.5: A cross sectional schematic of the pipe. A) The reflected light is distorted by the curved surface, B) the reflected light is not distorted by the curved surface due to presence of water-filled rectangular reservoir.

For each of the 25 different experimental conditions, about 9000 8-bit gray scale images were taken at a sampling rate of 30 Hz. The shutter pattern of the camera and synchronous laser pulses are displayed in Figure 2.6. Two lasers alternated in releasing one light pulse every camera frame. Both lasers individually pulsed at 150 μs intervals and the time separation between them was the time elapsed between each image pair. The

delay generator was used to control the timing of the laser pulses. In Figure 2.6, frames 1 and 2 are image pairs, and so are frames 3 and 4.

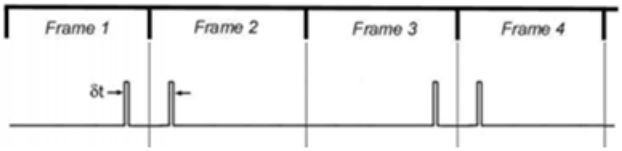

Figure 2.6: Camera and laser pulse synchronization pattern; the camera captures single frames over 15 μs intervals. This figure illustrates how the short laser pulses can have a time separation of δt. (Adapted from Dabiri, 2006)

A unique time separation between the images was set for each flow rate since it had the most dominant effect on the instantaneous particle velocities, and hence the particle shift in the image pair. If the time separation was too large, the PIV cross correlation analyses would not be functional. And if the time separation was too small, a spatial change would not be visible. By trial and error, the time separations of 2.22, 1.22, 0.5, 0.15 ms were set for the volumetric flow rates of 0.1, 0.2, 0.6 and 1 gpm, respectively. These time separations were programmed on the pulse generator for each condition.

Once the images were acquired, the velocity fields were computed by cross-correlating the image pairs. An in-house algorithm in the Heurisko domain was used. The first image of each image pair was partitioned into 32x32 pixel cells, called interrogation windows. An interrogation window was read as a gray scale value for each pixel in the cell, resulting in 32x32 two-dimensional scalar fields. In the second image of the image pair, a search region of 64 × 64 pixels was set for each corresponding interrogation window to search for the particles' movement between the two images.

A cross correlation [41] (see Equation 2.5) was implemented on the gray scale values of the 32x32 pixels in an interrogation window against the values of all 32x32 pixel cells in

the corresponding 64x64 search window. This resulted in a 32x32 discrete scalar field $R_{II}(x, y)$ for every interrogation window. The value of $R_{II}(x, y)$ at a certain location in an interrogation window could be attributed to the pixel at position x and y that was the center of a 32x32 pixel cell of the corresponding 64x64 search window. At the location in the second image where a group of particles in the first image had traveled to, the correlation coefficient had the largest magnitude, which appeared as a peak in the correlation scalar field. A displacement vector was drawn from this location to the center of the interrogation window. In every interrogation window there resided a single vector. This displacement vector was divided by the time separation in order to obtain a velocity.

$$R_{II}(x, y) = \sum_{i=-K}^{K} \sum_{j=-L}^{L} I(i, j) I'(i + x, j + y) \quad (2.5)$$

In Equation 2.5, $I(x, y)$ is the gray scale value for the pixels in the interrogation window and $I'(x, y)$ is the gray scale value for the pixels in a section of the search window. A scalar value with coordinates x and y rests at the center of every 32x32 section of a 64x64 search window. This equation sums the product of intensities of all pixel location pairs between a 32x32 interrogation window and a 32x32 pixel cell of the search window. A pixel-to-length conversion factor was used to covert the vectors into velocity units cm/s. In the given setup, the conversion factor was 0.0017 pixels per cm.

An image pair yielded one velocity vector field. Therefore, about 4500 vector fields were acquired for each experimental condition. Sporadically aligned vectors that were considered noise of the statistical cross correlation function were corrected using a local median test as proposed by Siddiqui et al. [32] that examined both magnitude and angular deviations of every vector against its eight neighbouring vectors. There was less than 1% of spurious vectors in the given velocity fields.

In some of the images, there were certain local regions with visual impedances that needed to be removed from the images. In particular alignments of the laser and camera, reflections disturbed the quality at certain locations within the image. These local regions only resulted in noisy data without contribution to the results. These bad regions were

marked out and the corresponding velocity vectors were excluded from subsequent analyses.

The images taken by the PIV setup encompassed a 3.5 cm long segment of the pipe. As a parcel of fluid passed through the test heat exchanger, it amassed an increasing amount of heat at a non-uniform rate. The axially varying heat transfer rates therefore caused the velocity profile to axially vary as well along the test heat exchanger. The entire heat exchanger was 0.9 meters, and it was assumed that the change in flow profile along the 3.5 cm section of acquired images was negligible. This was concluded by analyzing the average the streamwise velocity component at the far left and right columns and comparing them along each row. The case of lower flow rate and highest heating condition was considered for this analyses due to its maximized error contribution. It was found there was no noticeable change along the 3.5 cm long PIV image.

2.4 Error Analyses

As mentioned above, the uncertainty of all thermocouples used in this experiment was ± 0.5 C, as given by the manufacturer. Another source of error for the thermocouple measurements was the linear regression method used to calibrate the acquired voltage signals into temperature values. The condition considered for this evaluation held the highest applied error as calculated by the program Excel and was a value of approximately ± 1%, resulting in an uncertainty of ± 0.34 of the highest temperatures used in the present experiment. The total magnitude of this uncertainty was calculated with the following equation,

$$E_T = \sqrt{a^2 + b^2} \quad (2.6)$$

where E_T is the total uncertainty magnitude associated all thermocouples, and a and b are the manufacture and linear calibration uncertainties, respectively. Equation 2.6 resulted in a total uncertainty of 0.6 C for the thermocouples used to acquire temperature data in this thesis.

The error sources present in the PIV setup were the particle diameter, velocity gradient, peak locking and adaptive Gaussian window interpolation [33]. The glass particles used to reflect the laser light had a diameter of 15 μm, and hence 0.882 pixels. A correlation between particle diameter (measured in pixels), and the expected error was provided in Figure 5(a) of Cowen and Monismith [33], which was

$$\epsilon_{u_1} = (-0.03) + 0.095 = 0.065 \ \ pixels \qquad (2.7)$$

The source of error attributed to peak locking was approximated as a function of particle diameter, found in Figure 13 of Prasad et al. [34]. It was illustrated that a particle diameter of 0.882 pixels was attributed with an error of

$$\epsilon_{u_2} = (0.4)\epsilon_{u_1} = \ 0.025 \, pixels \qquad (2.8)$$

The error due to the PIV setup was based on the largest average velocity gradient present during experimentation. This was found to be approximately $\frac{\partial u}{\partial y} = 0.015$ pixels/pixel during conditions of maximal flow rate and any heating condition (due to similarity). Using Figure 5(e) in Cowen and Monismith [26], the error attributed to this velocity gradient was the sum of both mean and RMS errors, resulting in a total error of

$$\epsilon_{u_3} = (-0.01) + 0.03 = 0.02 \ \ pixels \qquad (2.9)$$

The error attributed to adaptive Gaussian window interpolation (AGW) was provided in Figure 5(f) of [33]. The total number of vectors fields used for analyses was 4500, which converted to an error of approximately

$$\epsilon_{u_4} = 0.08 \ \ pixels \qquad (2.10)$$

The total error associated with the PIV setup was calculated as follows,

$$E_{PIV} = \sqrt{\sum_{i=1}^{4} \epsilon_{u_i}^2} \qquad (2.11)$$

resulting in a total error of 0.11 pixels, which converts into 0.015 cm. This error value for the calculation of velocity vectors then translates into a velocity uncertainty of ± 0.015 cm/s.

2.5 Conclusions

An immersed pipe heat exchanger was constructed by completely submerging a pipe of flowing fluid into a stagnant, near-isothermal, hotter fluid. The underlying thermo-fluid processes were experimentally investigated by acquiring temperature and velocity measurements of the internal flow at a region located near the outlet of the heat exchanger. A thermocouple rake was built and used to acquire a temperature field in the internal cross-sectional plane of the pipe. Nine thermocouples were placed inside the pipe, and three were placed on the outer surface of the pipe at the same axial location; one on the top, one on the bottom and one on the side. Two additional thermocouples resided at the inlet and the outlet of the heat exchanger in order to measure the total heat transfer rate into the fluid through the stagnant secondary fluid.

Particle image velocimetry (PIV) was employed in the same axial region as the thermocouple measurements in order to acquire a velocity field of the internal flow. A laser illuminated micro glass particles in the flowing fluid, which was captured by a camera. These images were run through a cross correlation algorithm in order to obtain the velocity field. The outer rectangular reservoir in the test heat exchanger allowed for the acquisition of a non-distorted images.

Chapter 3

3 Temperature Field

As mentioned in Chapter 2, the temperature field inside the tube was measured using a rake of thermocouples. This chapter presents and discusses the fluid temperature behavior inside the test heat exchanger under various conditions.

3.1 Computation of physical and dimensionless parameters

The total amount of heat per unit time (q) transferred into the primary fluid was calculated using Equation 3.1, where T_{inlet} and T_{outlet} are the bulk fluid temperatures at the inlet and outlet of the test heat exchanger, respectively, $\dot{m}$ is the mass flow rate of the primary fluid and c_p is the specific heat of the fluid [35]. In the present study, time-averaged values of the inlet and outlet fluid temperatures were used in Equation 3.1, and c_p was computed at the mean of the average inlet and outlet temperatures.

$$q = \dot{m} c_p (T_{outlet} - T_{inlet}) \quad (3.1)$$

The Reynolds number defined in Equation 1.1 is a dimensionless quantity that determined the ratio between inertial and viscous forces acting on the fluid. Since the fluid density and viscosity depend on the fluid temperature, during fluid heating even at a given flow condition, the Reynolds number was expected to change along the pipe length as well as for different heating cases. To keep consistency for comparison purposes, the Reynolds number for each flow rate at room temperature was used as the reference Reynolds number throughout this thesis. For the flow rates considered in this study, the Reynolds number for the unheated cases varied from 330 to 6670.

The bulk temperature of the primary fluid at the cross-sectional plane of the temperature measurement was also calculated in order to determine the thermophysical properties of the fluid at this location. This bulk temperature was found by spatially averaging the fluid temperature at nine locations in the measurement rake (see Figure 2.3b). Various dimensionless parameters were calculated at this location as a reference for the

subsequent analyses of corresponding temperature and velocity fields. The Prandtl number (Pr) in Equation 3.2, is the ratio of viscous diffusion rate to the thermal diffusion rate, which was dependent only on the state of the fluid (thermophysical properties). The Nusselt number (Nu) in Equation 3.3 is the ratio of convective to conductive heat transfer rates normal to the boundary of the heated surface (i.e. the pipe). The Grashof number (Gr) in Equation 1.2 is the ratio of buoyant to viscous forces present on the fluid [1].

$$Pr = \frac{c_p \mu}{k} \qquad (3.2)$$

$Nu = \frac{hL}{k}$ (3.3)Certain assumptions were made in order to compute some of these parameters. The inner surface temperature of the glass tube was calculated using the measured outer surface temperature and a local heat flux density through the glass. The local heat flux q'' was approximated to be constant axially and circumferentially along the pipe in order to use the total heat transfer rate q to find the average heat flux through the entire pipe. The local heat flux could then be expressed as $q'' = q/A$, where A is the heat transfer surface area (an average of ID and OD of the pipe was used). This implied that the outer and inner surface temperature difference was constant everywhere on the pipe. The four outer surface locations in the measurement plane were spatially averaged to yield the average outer surface temperature. The approximate radial heat flux into the fluid at this location must initially have passed through the glass via conduction. Hence, knowing the conductive heat flux, the average inner surface temperature could be estimated by using Fourier's law of conductive heat transfer. The conductive heat transfer rate through a circular pipe of uniform heat flux was calculated as follows [35],

$$q = \frac{2\pi k L}{\ln\left(\frac{r_o}{r_i}\right)}(\mathrm{T}_{\mathrm{outer}} - T_{inner}) \qquad (3.4)$$

where q is the total heat transfer rate from Equation 3.1, r_o and r_i are the outer and inner radius of the glass pipe, L is the axial length of the heat exchanger, and T_{outer} and T_{inner} are the inner and outer glass pipe surface temperatures, respectively.

The radially averaged glass inner surface temperature and the bulk temperature of the fluid allowed for the calculation of the Grashof number and the approximate convective heat transfer coefficient *h*, which was then used to calculate the Nusselt number. Considering the one-dimensional heat transfer, the heat transferred through conduction via the glass pipe was equal to the convective heat transfer to the primary fluid inside the pipe. The convective heat transfer coefficient was calculated using Newton's law of cooling as presented in Equation 3.5, where T_{bulk} was the bulk fluid temperature in the temperature measurement plane and flux q'' was calculated using q in Equation 3.1.

$$h = \frac{q''}{T_{inner} - T_{bulk}} \quad (3.5)$$

Although for calculation simplicity, the heat flux through the glass tube was assumed constant throughout the entire test heat exchanger, in reality it varied both axially and radially. Hence, the dimensional and dimensionless parameters computed using this assumption can be treated as bulk parameters not local parameters. This issue is further discussed in detail in Section 5.2.

The above computed and measured parameters of the primary fluid in the measurement plane were used to calculate the discussed dimensionless quantities. Table 3.1 lists the values of the key parameters for the four extremum highest and lowest operating flow rate and bottom wall temperature conditions.

Again, the Grashof number quantifies the ratio of buoyant to viscous forces. It can be interpreted loosely as the natural convection analogue of the Reynolds number in forced convection (the ratio of inertial to viscous forces). As shown in Table 3.1, the Grashof number was higher at the higher bottom wall temperature due to the magnified buoyant forces. The results also show that at the same wall temperature, the Grashof number was relatively lower at the higher flow rate. This was due to the reason that an increase in the flow rate reduced the temperature difference between the pipe surface and the bulk fluid and hence, reduced the buoyant forces. Therefore, the highest value of the Grashof number ($Gr = 95{,}000$) was obtained at the lowest operating flow rate and highest bottom

wall temperature, and its lowest value ($Gr = 14{,}000$) was found at the highest flow rate and lowest bottom wall temperature.

The Reynolds number was primarily considered for the forced convection phenomena present in the experiments, while the Grashof number was considered for the natural convection phenomena present. During mixed convection, both forced convection and natural convection modes co-exist. The relative contribution of each mode during mixed convection was quantified using a dimensionless quantity Gr/Re^2 which represents the ratio of buoyancy to inertial forces. If $Gr/Re^2 << 1$, the forced convection mode dominates, while for $Gr/Re^2 >> 1$, natural convection mode dominates [2]. For $Gr/Re^2 \approx 1$, both modes have almost equal contribution. The values of Gr/Re^2 for the four extremum cases are also presented in Table 3.1. As the results show, the highest measured $Gr/Re^2 = 0.6$ was found at the highest wall temperature and lowest flow rate indicating that forced convection had a relatively higher contribution compared to natural convection, where the contribution of the latter was still significant. At the opposite conditions of lowest operating bottom wall temperature and highest flow rate, the smallest value of the ratio was found as $Gr/Re^2 \approx 10^{-4}$, where the buoyant forces were almost completely negligible.

3.2 Heat transfer rate in the test heat exchanger

Figure 3.1 illustrates the relationship between the Reynolds number, Re, and the total heat transfer rate, q, for each heating condition that corresponds to a constant local bottom surface temperature of the rectangular reservoir. The results show that at a given flow rate, the heat transfer rate increased with an increase in the wall temperature, as expected. At the lowest Reynolds number, the heat transfer rate increased from about 20 W to 160 W (a factor of 8) as the wall temperature increased from 30 ^{o}C to 70 ^{o}C, whereas at the highest Reynolds number, the heat transfer rate increased from about 60 W to 260 W (a factor of 4.3) over the same wall temperature range. The higher temperature rise at low Reynolds number could be due to the reason that at this Reynolds number, the flow was originally in the laminar range. As the temperature increased, the

buoyancy effects continued to become stronger. Buoyancy also induces turbulence, hence, with an increase in the buoyancy effects, the flow transitioned to turbulence at this low Reynolds number, which increased the heat transfer rate. At high Reynolds numbers, turbulence is dominantly due to the mean shear stress. Although the buoyancy does contribute, its effects were still relatively low; hence the increase in the heat transfer rate is relatively small compared to the low Reynolds number.

The change in the heat transfer rate over the given Reynolds number range showed a strong dependency on the wall temperature, i.e. the temperature of the reservoir fluid, particularly for higher Reynolds numbers. At low Reynolds numbers in the laminar range for the unheated condition, the heat transfer rate increased monotonically with an increase in the Reynolds number for all heating conditions. This was likely due to an increase in the fluid velocity, which increased the heat transfer coefficient. In the high Reynolds number range that corresponded to the turbulent regime, the heat transfer rate remained almost constant.

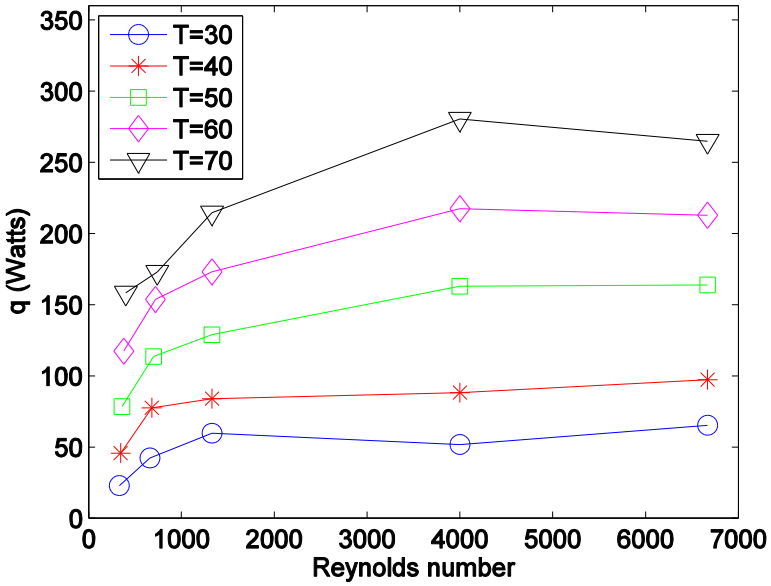

Figure 3.1: The total heat transfer rate versus the average Reynolds number along the test heat exchanger for various conditions. The curves represent conditions of constant bottom control temperature.

The results in Figure 3.1 showed that both the Reynolds number and the controlled wall temperature influenced the heat transfer rate. To investigate the relative influence of forced and natural convection on the heat transfer rate, the heat transfer rate was plotted versus Gr/Re^2 in Figure 3.2. The plot showed that the influence of Gr/Re^2 on the heat transfer rate was strongly dependent on the flow rate. That is, the influence of Gr/Re^2on the heat transfer rate increased with a decrease in the flow rate. At the lowest flow rate of 0.05 gpm, the plot showed a strong dependency of the heat transfer rate on Gr/Re^2. However, with an increase in the flow rate, the dependency became weaker and at the two highest flow rates, the heat transfer rate was independent of Gr/Re^2. At a given flow rate, the increase in Gr/Re^2 was due to the increase in the wall temperature. This effect was more pronounced at low flow rates, where the magnitude of $Gr/Re^2$was higher, i.e. the buoyancy effects were more significant compared to the inertial effects. However, as the flow rate increased, the buoyancy effects became weaker (smaller magnitudes of Gr/Re^2) and the heat transfer rate was dominated by forced convection.

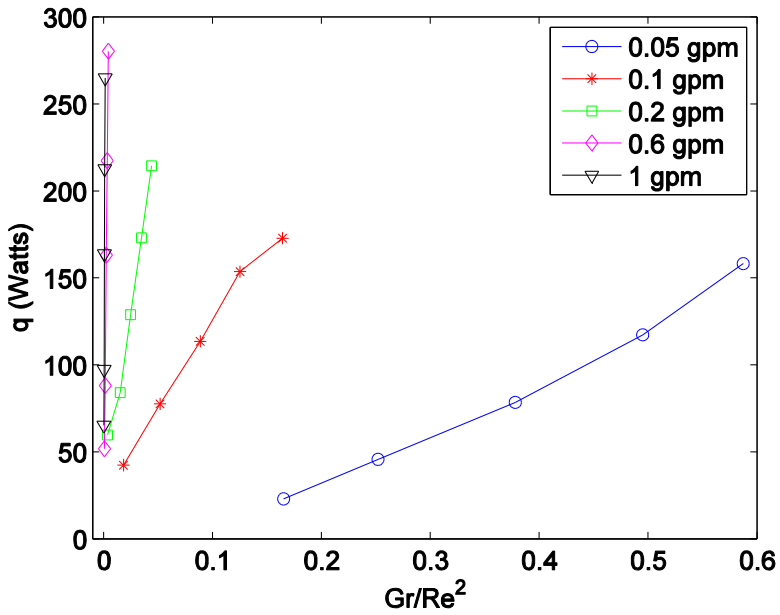

Figure 3.2: The heat transfer rate of the test heat exchanger versus the buoyancy-inertia ratio of Gr/Re^2. The curves represent constant volumetric flow rates.

3.3 Computation of thermophysical properties and dimensionless parameters

The Nusselt number (Nu) is often used as the dimensionless parameter to quantify the heat transfer process. According to [35], for forced convection in a fully developed pipe flow with constant local heat flux q'', the Nusselt number has a constant value of 4.36, independent of any parameters or thermophysical properties. The prediction of the local Nusselt number for the transition into, and fully turbulent flow was more difficult because it was dependent on certain parameters. The Gnielinski correlation [35] as presented in Equation 3.5 was used to predict the local Nusselt number for $Re > 3{,}000$ and uniform heat flux conditions.

$$Nu = \frac{\frac{f}{8}(Re - 1{,}000)\mathrm{Pr}}{1 + 12.7\left(\frac{f}{8}\right)^{0.5}(Pr^{2/3} - 1)} \qquad (3.5)$$

In the above equation, f is the friction factor of the pipe, which can be calculated for a smooth surface as follows [35].

$$f = (0.79\ln(Re) - 1.64)^{-2} \qquad (3.6)$$

Figure 3.3 depicts the relation between Nu and Re for both the laminar and turbulent regime. The curve generated from the Gnielinski correlation is also plotted within its bounds of accuracy for reference. At a given bottom wall temperature, the Nusselt number increased with an increase in the Reynolds number as expected. However, at lager Re in the turbulent regime, the graph showed a strong dependency on the bottom wall temperature, i.e. the secondary fluid temperature, which was not expected. It was observed that at a given Reynolds number in the turbulent regime, the Nusselt number decreased with an increase in the bottom wall temperature. At a given Reynolds number, as the wall temperature increased, the Grashof number increased, implying an increase in the contribution of buoyancy-driven natural convection. Hence, the results in Figure 3.3 indicated that the Nusselt number decreased with an increase in the Grashof number at a

given Reynolds number. In other words, in the turbulent regime, an increase in buoyancy dampened the turbulent convective heat transfer. A decrease in turbulent convection with an increase in the Grashof number was also observed by Gajusingh and Siddiqui [9]. It should be noted that at a given flow rate (especially at lower flow rates), an increase in the temperature also caused a minor increase in the Reynolds number due to a decrease in viscosity; this change was relatively small compared to the change in the Grashof number and hence for simplicity it was assumed to be constant.

The Gnielinski correlation is accurate for forced convection, which was relatively close to the values at the two lowest bottom wall cases where the buoyancy effects were negligible and forced convection was the dominant mode of heat transfer, as mentioned earlier. At $Re < 1000$, the Nusselt number values were relatively close to the theoretical value of 4.36. In the transition regime, the trends from the experimental results were quite different from the predicted values.

Volumetric flow rate (gpm)	Bottom wall temperature (C)	Reynolds number	Grashof number	Gr/Re^2	Nusselt Number
0.05	30	330	18,000	0.16	2.6
0.05	70	400	95,000	0.6	3.6
1	30	6660	14,000	0.0003	25.7
1	70	6660	68,000	0.002	10.2

Table 3.1: Dimensionless parameters are compared for the two extremum flow rates and two extremum temperatures, resulting in four separate conditions.

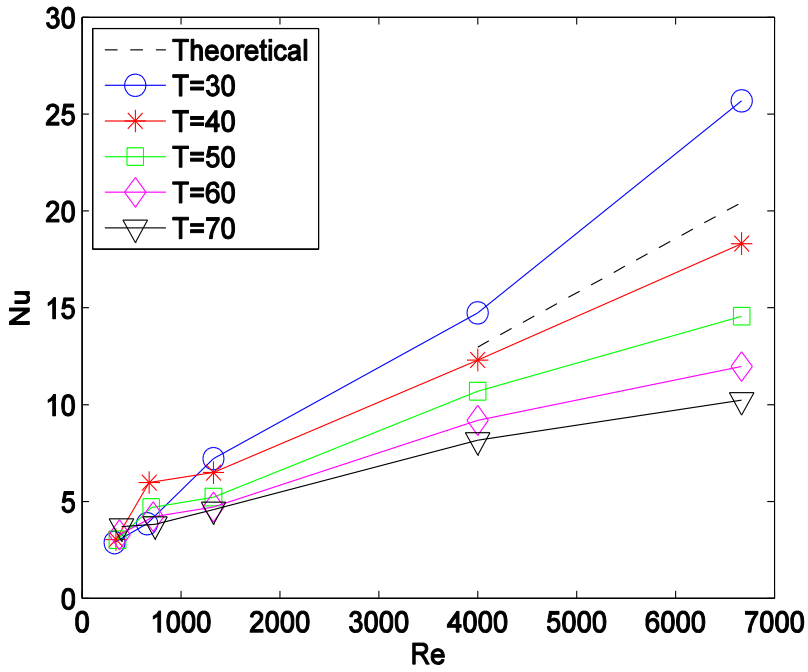

Figure 3.3 A theoretical correlation between Re and Nu compared for each curve of constant heating conditions.

The Nusselt number correlations are conventionally expressed for forced convection with a Reynolds and Prandtl number dependency, while for natural convection it is expressed with a Rayleigh number dependency. For mixed convection, where both forced and natural convection modes co-exists, none of these groups of correlations can accurately predict the Nusselt number. The combined effect of forced and natural convection can be conveniently shown by Gr/Re^2. Figure 3.4 shows the variation in the Nusselt number versus Gr/Re^2. The plot shows that the Nusselt number decreased with an increase in the Gr/Re^2, i.e. with a relative increase in the natural convection and/or a decrease in the forced convection. This was due to the reason that the rate of convection heat transfer was higher during forced convection compared to natural convection. This was likely due to a higher velocity magnitude during forced convection, which enhanced mixing. Figure 3.4 also shows that the dependency of Nusselt number on Gr/Re^2 was nonlinear.

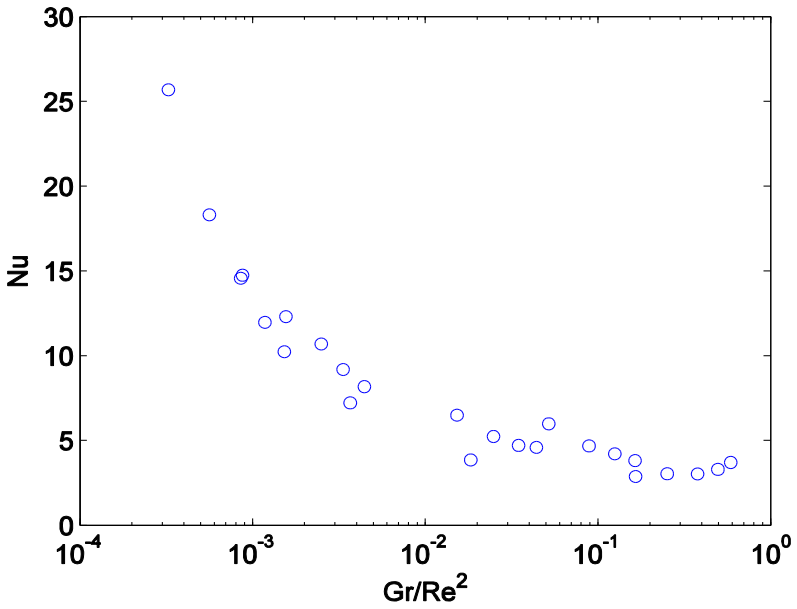

Figure 3.4: Nusselt number versus the buoyancy-inertia ratio for all 25 experimental conditions.

3.4 Temperature fields

The simultaneously acquired temperature data taken at nine locations in the measurement cross-sectional plane allowed for the investigation of the spatial temperature field. To study the spatial distribution of the temperature field in the pipe's cross-sectional plane, the results are presented in the form of colour maps. The spatial variation of the fluid temperature was most prominent at the highest bottom wall temperature, therefore the results are presented for this case in order to illustrate the underlying processes. Note that the trends were similar for other cases not presented here. Figures 3.5(a-e) present the cross sectional temperature fields for the highest operating temperature of 70 ^{o}C for five volumetric flow rates of $0.05, 0.1, 0.2, 0.6, 1\ gpm$. The corresponding Reynolds numbers for the unheated condition were 330, 670, 1330, 4000, and 6660, respectively. The inner and outer surfaces of the glass pipe are outlined in each figure with black for reference. The figures were not to physical scale; the boundary existed in the image in order to separate the internally placed thermocouples from the ones placed on the outer glass

surface. The bottom row of each figure represents the temperature of the boundary between the secondary fluid and the bottom aluminum plate. This temperature was different from the controlled surface temperature of 70 ^{o}C because it was on the top side of the material (the feedback thermocouple was on the dry bottom) and was at a different axial location.

It was seen in the first three images in this group of contour maps that there was a trend for the internal temperature to increase with height in the center vertical plane of the pipe. This temperature gradient became more prominent as the flow rate decreased. This was predicted by the corresponding Grashof numbers. Figure 3.5(a) therefore illustrated the largest temperature difference of about 13 ^{o}C between the top and bottom internal fluid temperatures at $Gr = 95{,}000$. The top and bottom outer surface temperatures remained hotter than the fluid close to the corresponding top and bottom inner boundary for all conditions as expected. The upper outer surface was typically hotter than the lower outer surface temperature. The side outer surface temperatures were lower than the top and bottom outer surface temperatures. The internal horizontal temperature center plane was approximately uniform with a slight tendency to maximize in the center and become cooler with increasing radial position.

The internal vertical temperature gradient was proposed to be present for the following reason. The temperature difference between the top outer surface measurement and the top inner fluid measurement was about 6 ^{o}C. The temperature difference between the bottom outer surface and the bottom fluid was 16.5 ^{o}C. This temperature difference was evidently much larger at the bottom than at the top. This result indicated that there was a larger heat flux through the bottom then there was through the top of the pipe in the measurement plane due Fourier's law of heat transfer. This was a result of the gravitational asymmetry of the flow geometry. The warmer fluid at the top formed a layer of stably stratified fluid, which restricted the fluid from mixing induced by buoyancy-driven convective flow and therefore unstable stratification was most prominent at the bottom of the pipe, where the hot fluid could rise. The relatively higher heat transfer rate at the bottom of the pipe indicated that the fluid was well mixed in this region, lowering its temperature compared to the top of the pipe where mixing was absent. The relatively

uniform fluid temperature in the mid-horizontal and lower half of the pipe indicated that the convective currents were mainly restricted in the lower half of the pipe.

In Figure 3.5(c) for $Re = 1330$, the cross sectional temperature field of the internal flow was more or less uniform, except for the top section of the pipe. The mid and bottom regions in the cross section for this flow rate was well mixed. The buoyancy-induced convection was absent in this region due to the absence of a vertical temperature gradient. At this Reynolds number of 1330, transitionally turbulent behaviour was visible from the high mixing rates and uniform temperatures, although it was not fully developed as shown by the upper higher temperature.

The vertical temperature gradient in the internal flow was almost negligible at the two highest flow rates of 0.6 and 1 gpm (Figures 3.5(d) and 3.5(e) for 70 ^{o}C). The corresponding Gr/Re^2 for these flow conditions were $\approx 10^{-4}$ and 10^{-3} respectively, which indicated a very weak buoyant force with respect to the inertial force. The uniform internal temperature implied that the fluid was undergoing an efficient mixing process other than the convection currents, namely the expected onset of turbulent flow. For the case of $Re = 4000$ and at 70 ^{o}C bottom wall temperature (Figure 3.5(d)), the plot showed that the primary flow was fully turbulent and the flow mixing extended over the entire pipe cross section leading to a uniform bulk temperature field. Similar results were observed at the highest Reynolds number of 6660.

The plots in Figure 3.5 also show a temperature non-uniformity along the outer circumference of the pipe. This was the surface that was in contract with the secondary fluid and was the heat source to the primary fluid. To investigate this temperature non-uniformity, the first step was to check whether this effect was driven by the vertical temperature variation in the secondary fluid. For this purpose, the secondary fluid temperature was measured at eight vertical locations from the bottom heated wall to the upper edge of the reservoir. The measurements were made in the same cross-sectional plane slightly off from the glass pipe for different conditions. Figure 3.6 shows the vertical temperature profiles of the secondary fluid for different Reynolds numbers at a bottom wall temperature of 70^{o}C. The results showed that the fluid temperature was

approximately constant over the vertical extent of the reservoir for each condition. This indicated that the variation in the pipe surface temperature was due to flow variations inside the pipe. In the following paragraph, a conceptual physical description of the heat transfer process in the test heat exchanger based on the temperature colour maps is presented.

As mentioned earlier, the flow dynamics of the primary fluid inside the pipe played an important role in the heat transfer along the pipes circumference at a given cross-section. These flow dynamics in turn were influenced by the thermal boundary conditions along the pipes circumference. Since the pipe was immersed in a fluid of higher temperature, the heat transfer occurred radially along the entirety of the pipes circumference. The local flow dynamics inside the pipe was influenced by the angular position at which the heat was transferred to the fluid from the inner pipe surface, due to the buoyancy effects. That is, the heat transfer through the pipe wall increased the temperature of the fluid parcels adjacent to the pipes surface. These fluid parcels then tended to rise vertically due to buoyancy inducing convective motion. These convective motions were well established in the bottom section of the pipe. However, as reaching the upper curvature of the pipe, due to the heat transfer from the upper section, the lighter fluid stayed at the top and thus, suppressed the convective motion, or mixing. As a result, the temperature of the fluid parcel in the top section of the pipe remained higher, which reduced the temperature differential across the pipe and hence, caused a reduction in the local heat transfer rate. This caused a local increase in the temperature at the surface of the pipe. In the bottom section on the other hand, the convective motion persisted, which took the warm fluid parcels away from the surface and brought the cooler and dense fluid parcels towards the surface. This process maintained higher temperature differential across the pipe and resulted in a higher heat transfer rate that caused a local reduction in the temperature at the surface of the pipe.

While the bulk temperature of the secondary fluid was relatively uniform over the reservoir height as shown in Figure 3.6, the variation in the local heat transfer rate at the boundaries of the immersed tube also caused local variations in the secondary fluid temperature in the peripheral region around the pipe. The secondary fluid in the reservoir

received heat from the bottom wall, which was then transported throughout the fluid domain. Since the dominant heat transfer to the primary fluid in the pipe was through the secondary fluid underneath the pipe, the convective motion in this region was expected to be very active. This convective motion brought the high temperature fluid parcels from the vicinity of the bottom heated wall to the region underneath the pipe. The fluid parcels rejected heat to the primary fluid via the pipe wall, which lowered the fluid parcels' temperature. The convective motion brought these lower temperature fluids parcels to the bottom plate and brought the high temperature fluid parcels to the pipe as mentioned earlier. A portion of this high temperature, low density secondary fluid tended to rise. But due to the presence of the top pipe surface, the fluid parcels tended to slide over the pipe curvature in the lower half. During this process, the fluid temperature dropped due to the heat transfer along the pipe curvature. Hence, the temperature at the mid-height of pipe was lower. Technically, these fluid parcels moving along the pipe curvature should have tended to rise to the top. However, due to the lower heat transfer rate at the upper section of the pipe (discussed earlier), the secondary fluid above the pipe remained at a higher temperature. This layer of high temperature fluid, with a density lower than that of the rising fluid parcels, prevented vertical fluid mixing and hence maintained a higher temperature. It was expected that this fluid layer received heat from the bulk secondary flow surrounding it at the same height.

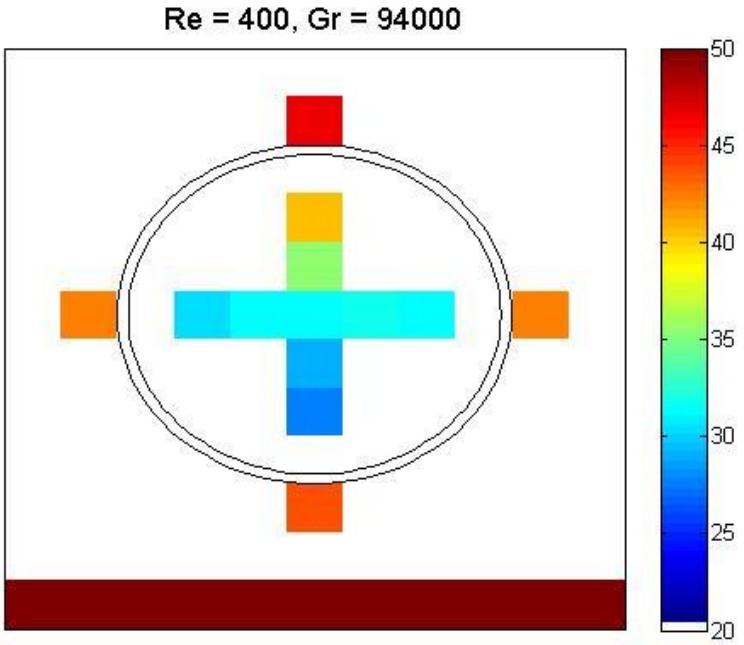
Re = 400, Gr = 94000
50
45
40
35
30
25
20

A.

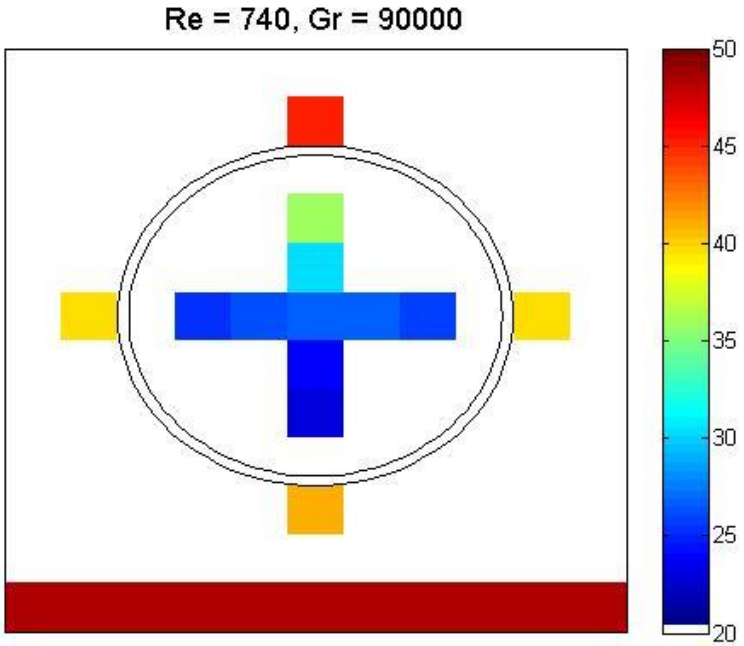
Re = 740, Gr = 90000
50
45
40
35
30
25
20

B.

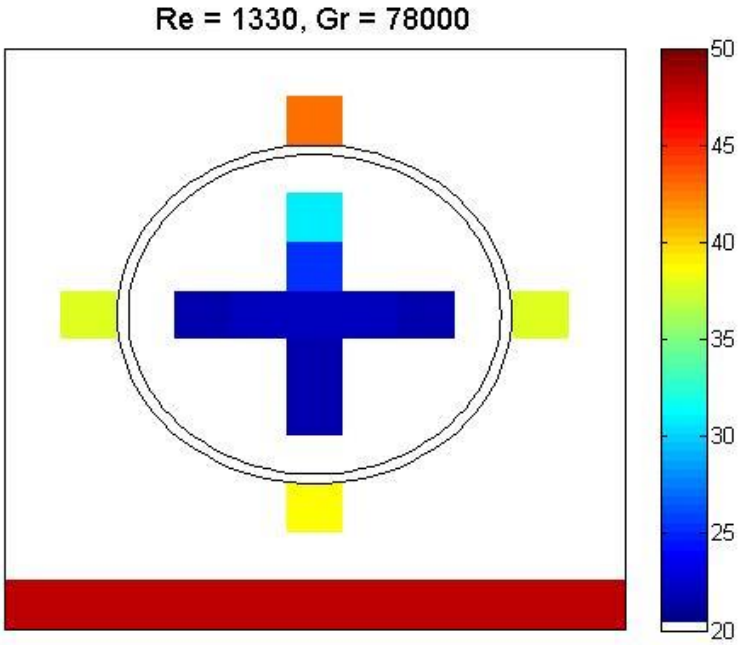
Re = 1330, Gr = 78000
50
45
40
35
30
25
20

C.

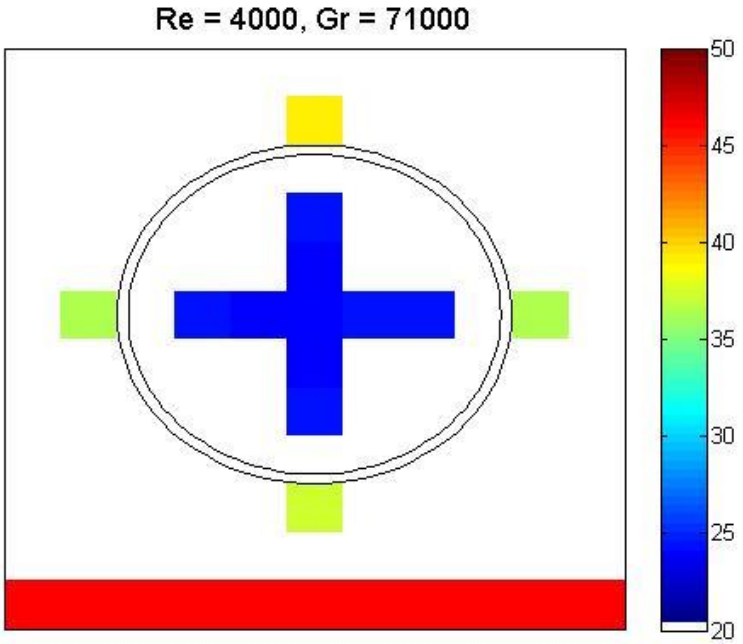
Re = 4000, Gr = 71000
50
45
40
35
30
25
20

D.

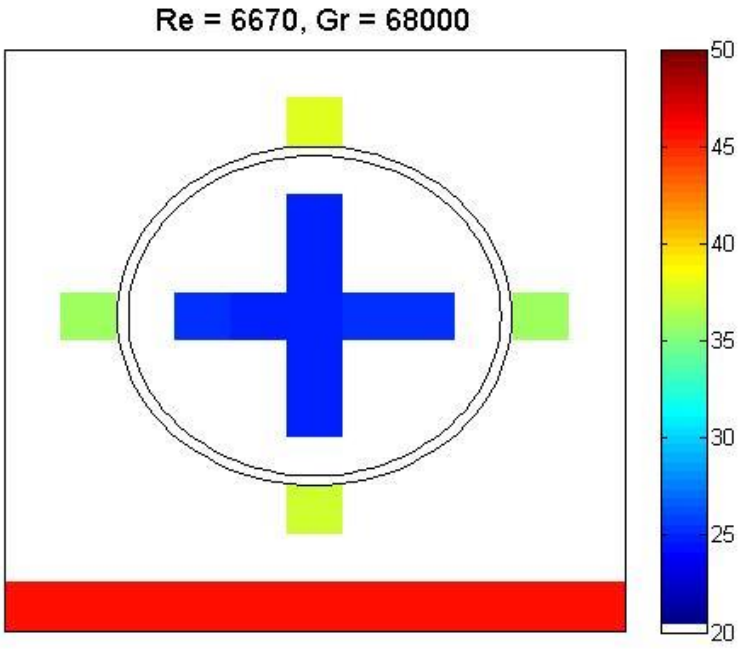

E.

Figure 3.5: Colour maps indicating the temperature field inside the temperature measurement plane during maximal bottom wall temperature of 70 ºC for the volumetric flow rates of A) 0.05, B) 0.1, C) 0.2, D) 0.6 E) 1 gpm.

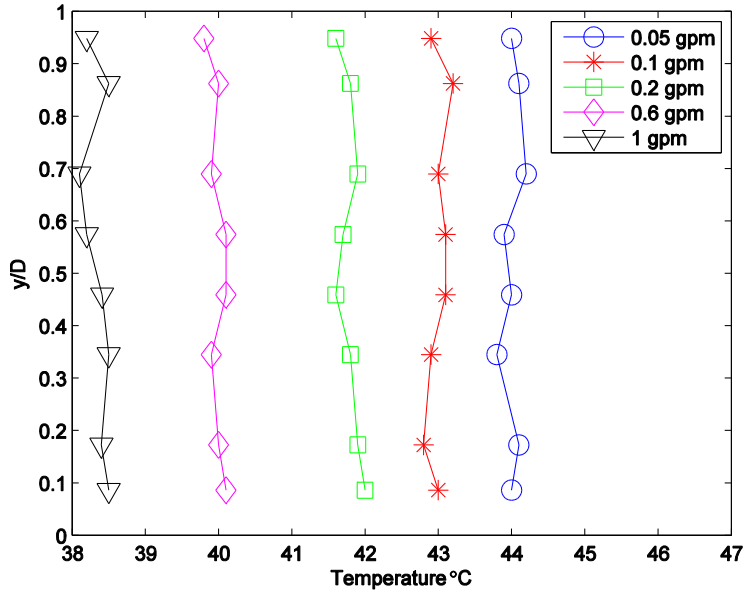

Figure 3.6: Confirmation of secondary fluid bulk temperature uniformity.

3.5 Vertical temperature profiles

The temperature field colour maps in the preceding section provide a good perception of the primary fluid temperature distribution in the cross-sectional plane of the pipe. For a detailed quantitative comparison of the fluid temperature variation under difference conditions, the vertical profiles of the fluid temperature was plotted in Figure 3.7(a-e). The graphs were separated for different flow rates, where each of the five heating conditions for the same flow rate was compared on the same graph. The height, y, is normalized by the inner pipe diameter, *D* and the normalized temperature Θ, is expressed by,

$$\Theta = \frac{T_{local}}{T_{bulk}} \qquad (3.7)$$

where T_{local} is the individual temperature acquired by a single thermocouple, and T_{bulk} is the average temperature of all nine thermocouples measuring the temperature in the cross-sectional plane of the pipe. The x-axis in Figures 3.7(a-e) were held consistent for the laminar flow regime, but not for the turbulent regime.

Figures 3.7 (a-c) show the temperature profiles at the flow rates that correspond to the originally laminar regime. A consistent trend in each of these graphs was observed, i.e. the fluid temperature increased from the bottom to the top of the pipe. However, the shape of the vertical temperature profile changed with a change in the bottom wall temperature. At the lowest bottom wall temperature of 30 ^{o}C, the vertical variation in the fluid temperature was very small (within approx. 10%) at all three lower flow rates (in the laminar regime). This was the case when the buoyancy forces were the weakest at each flow rate. The vertical temperature variations increased monotonically with an increase in the bottom wall temperature at each of these flow rates, i.e. higher vertical temperature gradients. The bulk temperature (i.e. $\Theta = 1$) occurred approximately at the center of the pipe for each case with a slight tendency to increase in height with flow rate due to the average change in temperature profile shape. The height of the mean

temperature seemed to be consistent within each flow rate, regardless of the heating condition. At a given flow rate, all curves converged to a point at approximately $\Theta = 1$.

As observed in the colour maps and profiles of the fluid temperature, the fluid in the top region was consistently hotter than the bottom region of the pipe. The plots in Figure 3.7(a-c) show that the fluid temperature in the pipe top region ranged from around 105% to 130% of the mean temperature. The fluid temperature in the bottom region however ranged from an average of 85% to 95% of the mean fluid temperature The Grashof numbers presented in Table 1 were highest for the lowest flow rate and highest bottom wall temperature at $Gr = 95{,}000$, indicating the highest average buoyant forces. This case was displayed in Figure 3.7(a) of $Re = 330$ and $T = 70\ C$, represented by a black curve. It presents the largest average deviation from the mean at this flow rate, indicating a higher heat transfer in the lower section and a lower heat transfer in the upper section of the pipe. The temperature difference between the top and bottom were measured at a maximum of 13 ^{o}C. The trend was similar at the next higher flow rate of Re = 670.

As the Reynolds number further increased to $Re = 1330$, the temperature profiles gradually started to become more uniform in the bottom half of the pipe, in particular at the higher wall temperatures (see Figure 3.7 c). However, the strong temperature gradients remained in the upper half of the pipe. This indicated that an increase in the flow rate enhanced mixing in the lower section of the pipe but the stably stratified layer in the upper section of the pipe remained strong enough to dampen convective motions attempting to penetrate into this layer. The difference in temperature between the fluid at the top and bottom of the pipe had decreased to 7.1 ^{o}C in this case at the highest wall temperature of 70 ^{o}C.

As the Reynolds number further increased and the flow regime transitioned to turbulence, the inertial effects became strong enough to overcome the damping due to stable stratification, and the flow mixing extend over the entire vertical extent of the pipe cross-section. As a result, the vertical temperature profiles became almost uniform (see Figure 3.7 d-e). The plots showed that the vertical temperature fluctuations were within 1-2% of the mean fluid temperature. The five temperature profile curves for each of the two high

Reynolds number cases were consistently partitioned into two groups. The two lowest operating bottom wall temperatures of 30 and 40 ^{o}C were both very uniform, presenting no obvious temperature trends. The higher operating temperatures of 50, 60 and 70 ^{o}C however, show a tendency to be warmer on the perimeter of the pipe and cooler in the center.

To better understand the relative contributions of buoyancy and inertial forces on the vertical temperature distribution inside the pipe, the vertical temperature profiles are plotted versus Gr/Re^2 in Figure 3.8. The partition between laminar and turbulent regimes is clearly evident in this figure. As observed, the vertical stratification was highest at the highest value of Gr/Re^2. As the ratio started to decrease, i.e. the buoyancy effects decreased relative to the inertial effects, the stratification effects started to reduce due to mixing beginning in the bottom section of the pipe, which was subjected to the strongest convective motions. The results also showed that the profiles in the upper section of the pipe remained almost the same at the two highest values of $Gr/Re^2 = 0.6$ and 0.1. These were the two cases at which the buoyancy effects were still relatively significant. A similar trend was observed at $Gr/Re^2 = 0.03$ where the buoyancy effect was expected to be very weak, however the profile in the upper section of the pipe started to move towards uniformity. This indicated that in the case of circumferential heat transfer, the stably stratified layer persisted even when the buoyancy effects became relatively very weak. The two lowest Gr/Re^2 values of 0.002 and 0.0003 were more or less uniform at $\Theta = 1$ throughout the height of the pipe, indicating that the buoyancy effects were almost negligible and inertial effects were dominantly inducing mixing throughout the pipe cross-section.

The laminar profiles closely resembled one another in that their normalized gradients were approximately similar along the height. Within slight deviations, the temperature of the fluid located at the bottom of the pipe deviated further from the mean with increasing Gr/Re^2, while maintaining the rest of the temperature profile. The condition of greatest $Gr/Re^2 = 0.6$ therefore indicatively had the largest average relative gradient throughout the height of the pipe, which continued to reduce with reducing Gr/Re^2. Both turbulent conditions were expectantly seen to be approximately uniform at $\Theta = 1$. The

relative variations in these profiles appeared negligible when compared to the large laminar gradients.

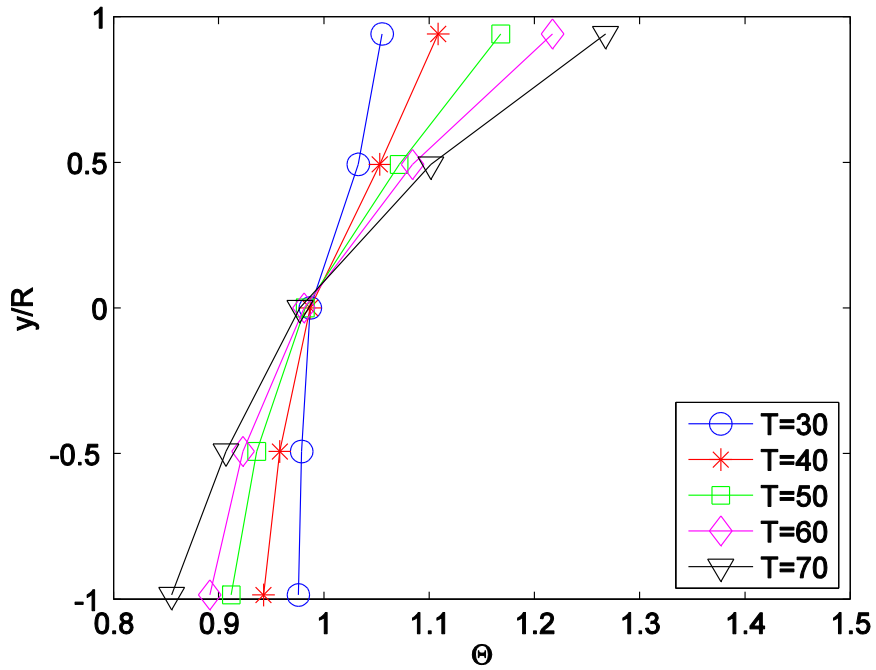

A.

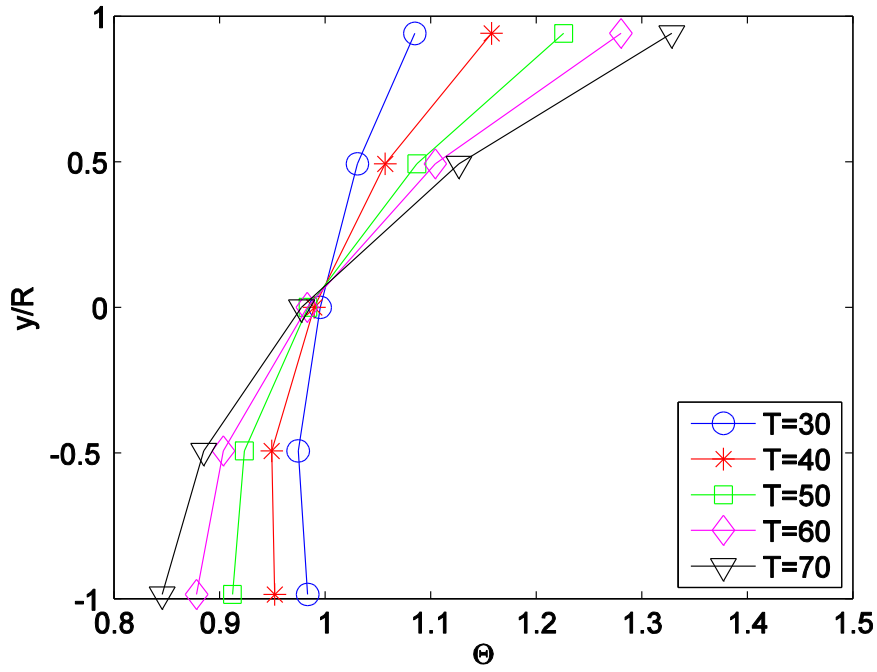

B.

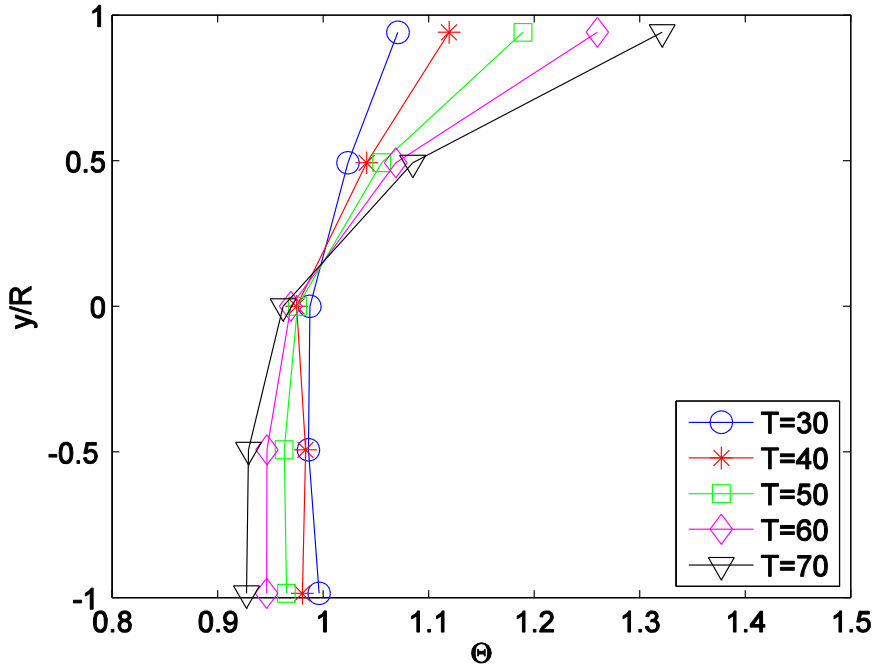

C.

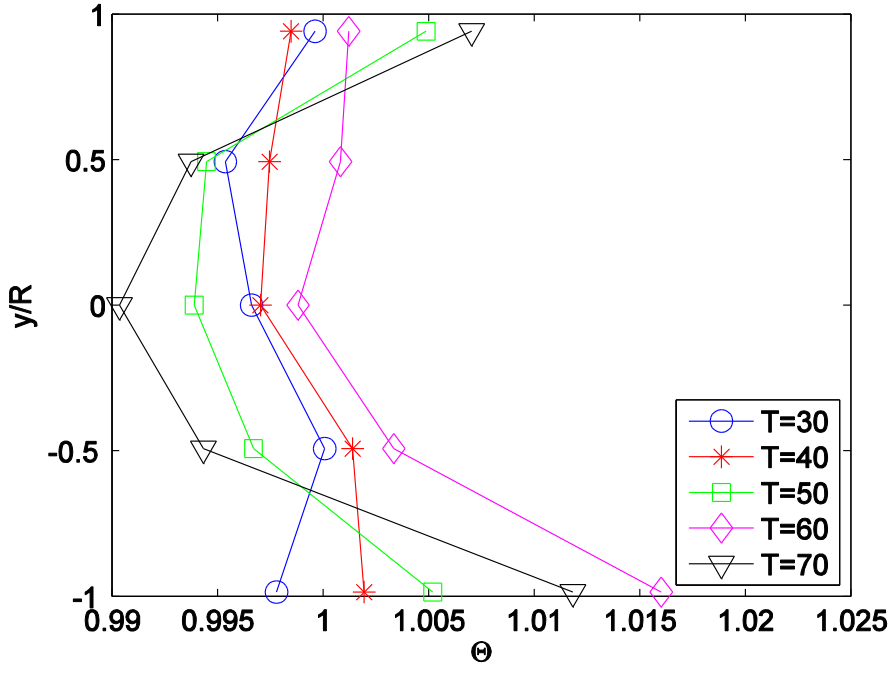

D.

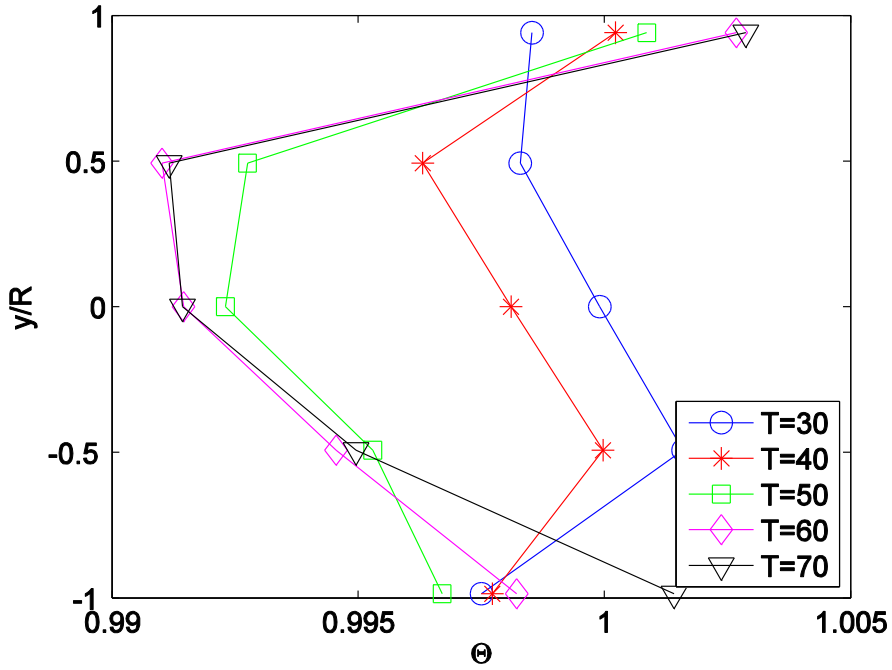

E.

Figure 3.7: Normalized temperature profiles plotted along the normalized height of the pipe. The volumetric flow rates are A) 0.05, B) 0.1, C) 0.2, D) 0.6, E) 1 gpm.

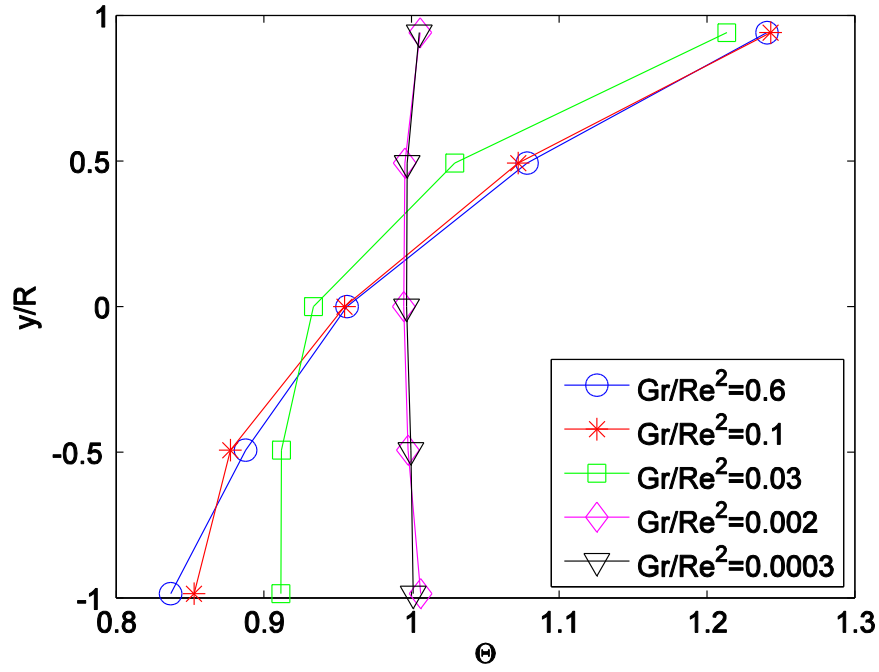

Figure 3.8: Normalized temperature profiles plotted along the normalized height of the test heat exchanger for interval buoyancy-inertia ratio values.

3.6 Conclusions of this chapter

This chapter investigated the temperature field in the cross-sectional plane of a horizontal pipe fully submerged in a hotter fluid subjected to different heating conditions over a range of flow rates. A thermocouple rake was constructed and inserted into the pipe in order to measure the temperature fields. With these acquired temperature values, the local heat flux through the pipe and primary dimensionless parameters were calculated. It was expectantly found that the outlet temperature of the test heat exchanger decreased with an increase in the Reynolds number, and also increased in an increase in the Grashof number. This was attributed to the relative and absolute magnitudes of forced and natural convective modes of heat transfer. It was found that this buoyancy-inertia ratio had a large dependence on the heat transfer rate of the fluid that increased as the flow rate decreased.

For initially laminar flow, the calculated Nusselt numbers approximately followed the Gnielinski correlation, which expressed Nu as a function of the Reynolds and Prandtl numbers, as well as the coefficient of friction of the pipes inner surface. In addition the present results also showed that the Nusselt number was dependent on the heating conditions, i.e. decreasing with an increase in bottom wall temperature, except for very small Re. In other words, as the magnitude of the natural convection mode increased at a given Re, the turbulent convective heat transfer rate decreased. The Nusselt number was also found to be negatively and non-linearly correlated with the buoyancy-inertia ratio, implying the rate of convective heat transfer was larger during forced convection compared to natural convection.

At low flow rates that correspond to laminar flow regime in the absence of heating, it was observed that a strong vertical temperature gradient existed in the pipe cross-sectional plane. This temperature gradient (cooler at the bottom, and hotter at the top) increased in magnitude with an increase in Gr/Re^2. The temperature gradient was prominently attributed to the asymmetric convective behaviour present inside the pipe; natural convection was prominent in the bottom region due to unstable stratification, while

absent in the top region due to stable stratification. The unstable stratification in the bottom region induced convective motions that were responsible for the larger heat transfer rate through the bottom of the pipe, compared to the top. With an increase in Reynolds number that transitioned the flow into the turbulent flow regime, the temperature profiles became relatively uniform in the pipe cross-sectional plane and the local convective motions due to unstable stratification became negligible. This was expected due to efficient fluid mixing induced by turbulence.

Chapter 4

4 Particle Image Velocimetry

As mentioned in Chapter 2, the instantaneous velocity fields inside the tube were measured using the particle image velocimetry (PIV) technique at the same location as the temperature field measurements. This chapter presents and discusses the flow behavior inside the test heat exchanger under various conditions.

4.1 Instantaneous Velocity Fields

Figure 4.1 illustrates a typical instantaneous velocity field at $Re = 670$ and a bottom wall temperature of 60 C. The figure shows a relatively well-organized flow in the streamwise direction with negligible fluctuations. The velocity vectors in the immediate vicinity of the walls were generally masked due to vision obscurities and hence, the convergence of the flow velocity field to zero at the top and bottom walls is not visible in Figure 4.1. The change in velocity outwards from the wall had some resemblance to that of typical Poiseuille flow, however, a clear asymmetry along the pipe height is evident in the figure. That is, the maximal fluid velocity was in the lower section of the pipe, not at the center (as for the Poiseuille flow). This effect will be discussed in details in the later part. The void in the middle of this figure was due to the masking out of the high uncertainty data caused by the reflections in the PIV images. All other laminar cases are qualitatively similar to the one presented, with minor variations.

The reason for the vertical asymmetry in the flow profile is proposed as follows. In the previous chapter, a temperature gradient was present in the vertical cross sectional profile of the temperature measurement plane. The temperature of the fluid was minimal at the bottom of the pipe, and increased with height. It was concluded that this temperature gradient persisted due to buoyantly driven mass transfer from bottom to top. Typically, when the fluid is hotter, its viscosity decreases, which therefore decreases the wall friction. The hotter fluid therefore has less friction and should move faster. Instead, the velocity profile indicated that the velocity of the fluid was highest in the lower, colder region of the pipe. This was probably because the top region of the pipe restricted the

present convective behaviour, increasing the static pressure and impeding horizontal movement. At the bottom of the pipe, where the fluid was free to upwardly convect out of and into the upper region, the static pressure dropped and the fluid flowed more freely. This convective behaviour therefore forced the velocity profile to shift its peak into a colder, lower region of the pipe opposed to residing at the center, as seen in Figure 4.1.

As discussed in the previous chapter, the convective behaviour of the fluid influenced the heat transfer rate through the glass pipe to be higher through the bottom than through the top of the pipe. In turn, this behaviour forced a change in the velocity profile of the pipe, increasing its velocity in the lower region. This phenomena even further increased the difference in heat transfer rates between the top and bottom of the pipe by increasing the mass carried away by forced convection, opposed to natural convection as discussed above. The non-uniform circumferential heat transfer rate into the fluid was then much larger than qualitatively predicted from the previous chapter on natural convection.

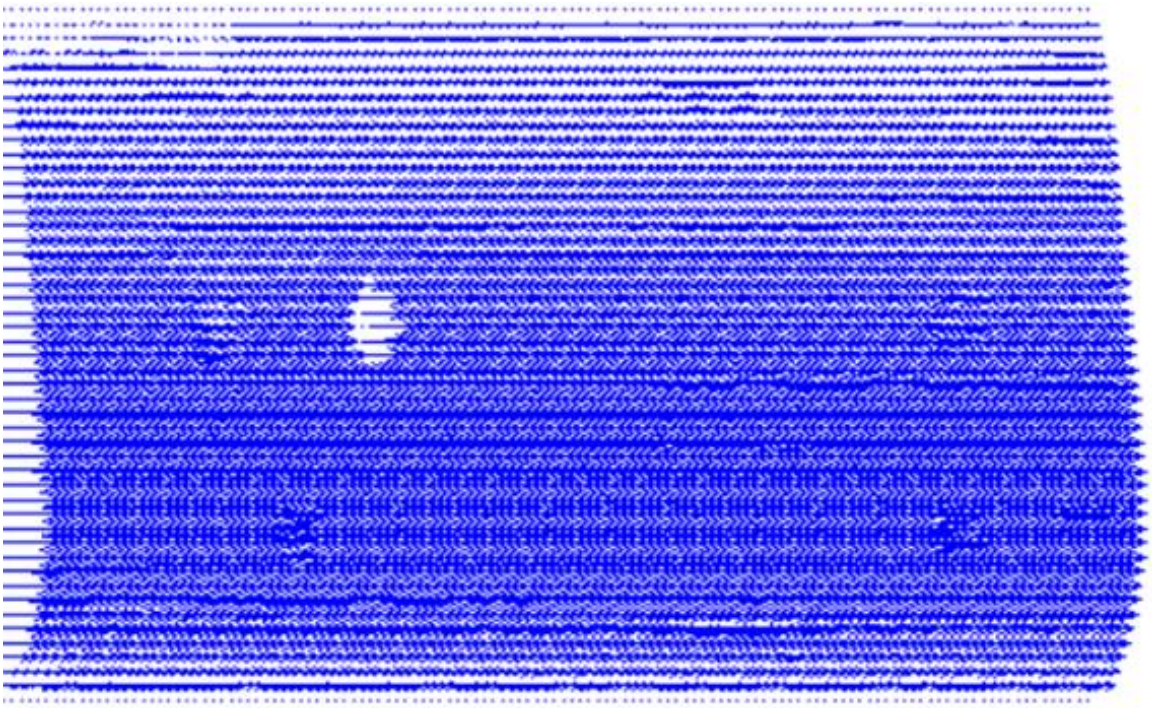

Figure 4.1: PIV acquired instantaneous laminar velocity vector field

The planer PIV images as in the present study provide a sequence of instantaneous velocity fields at a particular experimental condition. For a given case, the mean velocity field is obtained by time-averaging the instantaneous velocities at each grid point. The turbulent fields are obtained by subtracting the mean velocity at each grid point from the corresponding instantaneous velocities. That is,

$$u'(x,y,t) = \tilde{u}(x,y,t) - U(x,y) \quad (4.1)$$

where u' is the turbulent velocity, $\tilde{u}$ is the instantaneous velocity, U is the mean velocity, *x* and *y* are the coordinate of the grid point and *t* is the time. Figure 4.2 illustrates a typical turbulent velocity field at $Re = 6670$ and bottom wall temperature of 60 C. When heat is added to a fluid flow from the bottom, thermal plumes of warmer and less dense fluid are formed and ascend into the main flow, which are replaced by the falling parcels of cooler and denser fluid from above. These flow patterns are typically observed in pure natural convection [36, 37] as well as in mixed convection when Gr/Re^2 is significantly higher than unity [38]. In the present case, the value of Gr/Re^2 was 0.0003, which was significantly less than unity. Hence, the buoyancy-induced flow was very weak and the turbulence was predominantly due to the mean shear. Thus, the flow features evident in the Figure 4.2 are associated with the classical turbulent flow in a pipe, which include bursting and sweeping motions, local vortices, etc. These turbulent flow patterns play a very critical role in the transportation of heat from the wall into the fluid domain as well as in fluid mixing. Both of these processes increase the rate of heat transfer. The results in Figure 4.2 also show that the turbulent velocity field was relatively similar from top to bottom of the pipe indicating that the turbulence was fully spread out across the pipe. This caused fluid mixing across the pipe cross-section which resulted in an almost uniform fluid temperature over the height, which was evident in the corresponding fluid temperature profile in Figure 3.7. More detailed analyses of the turbulent velocities is presented later in this chapter.

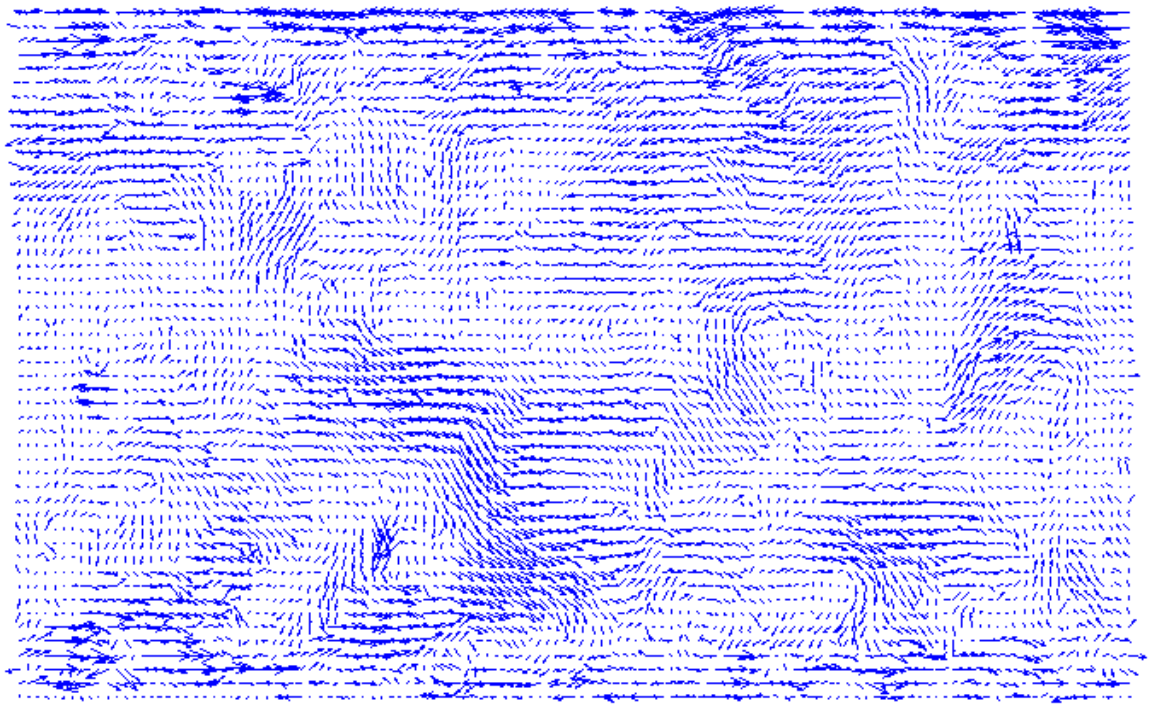

Figure 4.2: Instantaneous turbulent velocity field u' at Re = 6670 and bottom wall temperature of 60 C.

4.2 Mean Velocity Profiles

As mentioned earlier, the mean velocity field, $U(x, y)$ was computed by time-averaging the corresponding instantaneous velocities. The two-dimensional mean velocity field was then spatially averaged at each height to obtain the streamwise-averaged mean velocity profile, $\overline{U}(y)$, as a function of height. Figure 4.3 shows the vertical profiles of the mean streamwise velocity ($\overline{U}$) at different heating conditions and flow rates. The profiles were normalized by the streamwise velocity averaged over the pipe cross section, $\overline{U}$, for the corresponding condition, while the height is normalized by the pipe diameter. Figure 4.3(a) shows the mean velocity profiles at the lowest flow rate of 0.1 gpm for different wall heating conditions. The flow in the absence of heating at this flow rate was in the laminar regime where the pipe flows exhibited classical Poiseuille velocity profiles. The results in the plot showed an asymmetry in the profile with the peak velocity shifted towards the bottom, which was a clear deviation from the Poiseuille behavior. This

indicated that under these conditions, wall heating influenced the mean flow structure inside the pipe. The plot also showed that the profiles at different wall heating conditions collapsed in a narrow band indicating that the change in temperature of the pipe wall due to the change in the surrounding fluid temperature does not have a major influence on the shape of the profile, except near the bottom end of the tube. It was also observed that the peak velocity magnitude was approximately 40% larger than the mean velocity. For the four heating conditions presented in the figure, the Gr/Re^2 values ranged from 0.02 to 0.08, which was within the same order of magnitude, hence the velocity profiles for different heating conditions showed a similar behavior. Figure 4.3(b) showed the mean streamwise velocity profiles at the flow rate of 0.2 gpm, which was also in the laminar regime for unheated condition. The shape of the profiles at this flow rate for different heating conditions was similar to that observed in Figure 4.3(a). The Gr/Re^2 for these cases has a relatively small range from 0.01 to 0.04, again supporting their similar profile shape. Figures 4.3 (c) and (d) illustrate the mean streamwise velocity profile at flow rates of 0.6 and 1 gpm. The flow at these flow rates in the absence of heating was in the turbulent regime. The results in both figures showed almost symmetric profiles, which were typical of the turbulent pipe flow. The effect of heating on the mean velocity was very weak for 0.6 gpm, which became negligible as the flow rate increased to 1 gpm. The Gr/Re^2 value for these cases ranged from 0.0003 to 0.002. The results showed that the peak velocity magnitude in these cases was about 15% larger than the mean velocity.

The velocity profiles at the two lower flow rates displayed in Figures 4.3 (a) and (b) had a slightly different relative shape, as did the profiles at the two higher flow rates shown in Figure 4.3 (c) and (d) under the turbulent conditions. This issue is further investigated. Figure 4.4 illustrates the normalized mean streamwise velocities for the same intervals of Gr/Re^2 as discussed in Chapter 3 for the temperature analyses. The two cases of $Gr/Re^2 = 0.1$ and 0.03 were at low Reynold numbers, the laminar flow regime under unheated conditions, while the cases of 0.002 and 0.0003 were at a high Reynolds number that corresponded to the turbulent flow regime under unheated conditions. The plot showed a clear change in the mean velocity behavior when Gr/Re^2 became very low. The case of $Gr/Re^2 = 0.1$ showed an increase in the velocity gradually from the

top of the pipe towards the bottom with the peak at approximately $y/D = 0.3$, indicating a higher normalized velocity in the top-mid region of the pipe relative to the case $Gr/Re^2 = 0.03$, which had a more uniform gradient from the top of the pipe to the peak of the profile at approximately $y/D = 0.25$. Although the absolute velocity gradient was much larger for the lower Gr/Re^2 values, the relative gradient seemed smaller on average in this top-mid region. The maximal velocity for the case of $Gr/Re^2 = 0.1$ was slightly higher along the height of the pipe than the lower case of $Gr/Re^2 = 0.03$. As mentioned earlier, the inertial effects started to become significant as Gr/Re^2 became less than unity. The results in Figure 4.4 showed an asymmetry in the mean velocity profile even at $Gr/Re^2 = 0.03$, where the buoyancy effects were significantly lower compared to the inertial effects. This indicated that the shape of the mean streamwise velocity profile was also influenced by the nature of the flow rate regime in the absence of heating. That is, in the flow regime that was in the laminar range in the absence of heating, the wall heating had a profound effect on the mean flow structure even when the buoyancy effects were relatively weak.

Other studies have also reported an asymmetry in the mean streamwise velocity profile at low Reynolds numbers in the presence of heating. Sookdeo and Siddiqui [21] reported an asymmetry in the mean velocity profiles in a flat-plate solar collector tube where the peak velocity shifted towards the bottom. The Reynolds numbers at room temperature were ranged from 150 to 900, all in the laminar regime. Depending on the heating condition and the flow rate, the location of the peak mean velocity ranged from $0.25 < y/D < 0.4$, which was consistent with the present results. The values of Gr/Re^2 in their study covered a very wide range from 0.7 to 511 indicating that the mixed convection in their case was predominately in the natural convection mode. Ouzzane and Galanis [39] in their numerical study of flow in an inclined tube with longitudinal fins heated from above, also observed an asymmetry in the mean velocity profile with the peak shifted towards the bottom side. They conducted simulations at $Re = 400$ and $Gr/Re^2 = 1.9$. They attributed the shift in the velocity peak to the secondary flow induced by buoyancy.

Figures 4.5(a,b) present the mean vertical velocity (v) normalized by the characteristic velocity scale $\overline{U}$ for the two laminar flow rate only, at different heating conditions

(corresponding to the cases presented in Figure 4.3 a & b, respectively). The manifestation of the mean vertical velocity in a horizontal pipe was due to the buoyancy-induced flow which acted parallel to the gravity vector. This resulted in the magnitude of the vertical velocity component being significantly lower than that of the streamwise velocity component at both flow rates. This indicated that the buoyancy effects (vertical flow) were much weaker than the inertial effects (streamwise flow), which was confirmed by the values of Gr/Re^2 less than unity at both flow rates. The positive sign in the figure indicates an upwards velocity opposed to a negative sign corresponding to a downward velocity. Although it is weak, the figures did illustrate the presence of convectively induced flows in each condition. Both figures showed relatively much stronger magnitudes of upward flow in the bottom region of the pipe that corresponded to the upward convective currents, indicating that natural convection was present in the bottom region of the pipe, and not in the upper region. The results also showed that at a given flow rate, the velocity profiles at different heating conditions were very similar. The profile shapes however showed some differences between the two flows. This showed that the change in the buoyancy effects due to the change in the wall temperature at a given flow rate had a relatively weak contribution compared to that of inertia due to the change in the flow rate. There was also a slight trend for the fluid in the top region of the pipe to have a downwards velocity, hence the negative value of v. This trend was slightly more prominent for the case of lower flow rate. This was likely due to the influence of the convective currents, which also had a downward component to satisfy mass conservation. It was also observed that the peaks of the mean upward velocity profiles were located at approximately the same height inside the pipe as the peak for the mean streamwise velocity profiles. This means that the location of maximal inertia also exhibited maximal buoyancy.

The vertical velocity profiles illustrated in Figure 4.5(b) were much less smooth than the velocity profiles at generally lower Reynolds numbers as seen in Figure 4.5(a). This ‘choppiness’ might have been a sign of the onset of turbulent behaviour that distorted the vertical velocity profile. For the fully turbulent conditions, the mean upward velocity vanished throughout the height of the tube; the turbulent flow behavior will be discussed in a later section.

These mean velocity results in combination with the corresponding temperature fields provided an insight into the underlying physical processes inside the pipe subjected to peripheral heating from a surrounding isothermal fluid. Both velocity and temperature results showed very distinct velocity and temperature fields for originally laminar and originally turbulent flow regimes (in the absence of heating). For the turbulent case (two higher flow rates), the results showed that the fluid temperature was almost uniform throughout the pipe cross-section. This indicated that the fluid was well mixed, which was confirmed by the mean velocity profiles at these flow rates that showed almost symmetric behavior about the pipe centerline. For the laminar case (two lower flow rates), significant variations in both velocity and temperature fields were observed with respect to the pipe height. The results in Figures 4.3 and 4.4 showed that at low flow rates, wall heating influenced both the streamwise and vertical velocity components. It was observed that both velocity components peaked in the bottom region of the pipe while the velocity magnitudes in the upper region were very small (up to an order of magnitude smaller than the peak magnitudes). This implied that the primary fluid in the pipe was moving much faster in the lower section of the pipe with higher mixing due to the vertical velocity component, compared to that in the upper section of the pipe. The corresponding fluid temperature profiles showed higher temperature and temperature gradients in the upper section of the pipe and relatively lower temperature and smaller temperature gradients in the lower section.

Based on these results, the underlying physical process at low flow rates could be described as follows: The peripheral wall heating induced convective currents in the lower section of the pipe. The overall effect of these convective currents was a rise in the warmer fluid from the wall region into the bulk fluid domain. While rising, these warm fluid parcels were subjected to a strong streamwise flow that pushes them in the downstream direction. As a result, these fluid parcels ascended at an inclination angle in the bulk fluid stream and hence penetrating into the downstream flow. This process enhanced fluid mixing, which reduced the vertical temperature gradient. The presence of both streamwise and vertical velocity peaks in the close vicinity of the bottom wall indicated that the warm fluid parcels rapidly moved away from the wall, which maintained a lower fluid temperature that enhanced the heat transfer rate. In the upper

section of the pipe, the lower magnitude of streamwise vertical velocity and almost negligible vertical movement caused the fluid parcels in that region to remain unmixed and to slowly move along the pipe. In the absence of mixing, the warm fluid parcels remained in the same configuration relative to pipe wall and hence, strong vertical temperature gradients were established with higher temperatures. The slow movement of these fluid parcels increased their contact time with the heated wall, causing some increase in the fluid temperature, but their persistent contact with the wall reduced the temperature difference required for a higher heat transfer, resulting is a much lower heat transfer rate compared to that from the bottom wall.

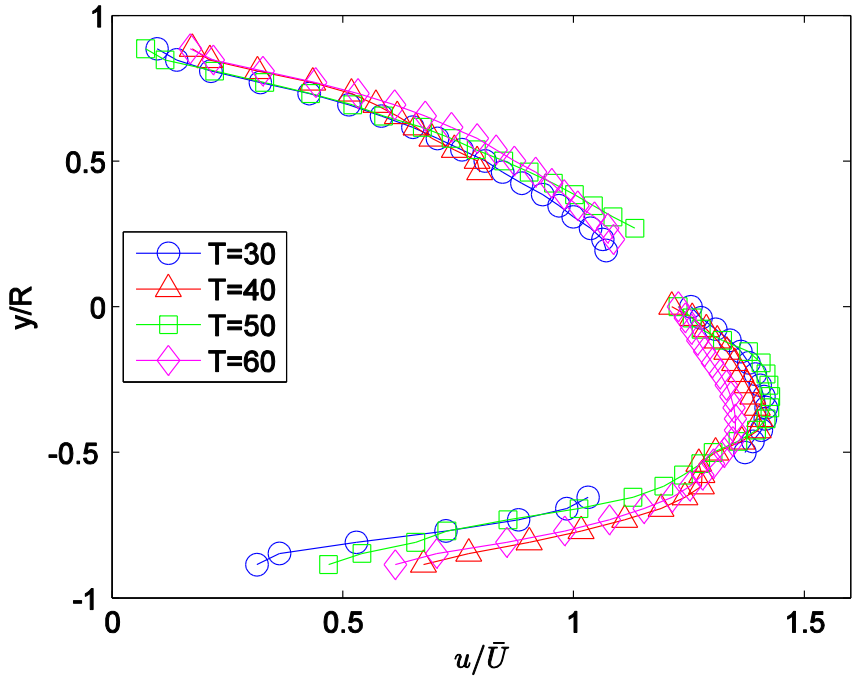
T=30
T=40
T=50
T=60
y/R
$u/\bar{U}$
1
0.5
0
-0.5
-1
0
0.5
1
1.5

A.

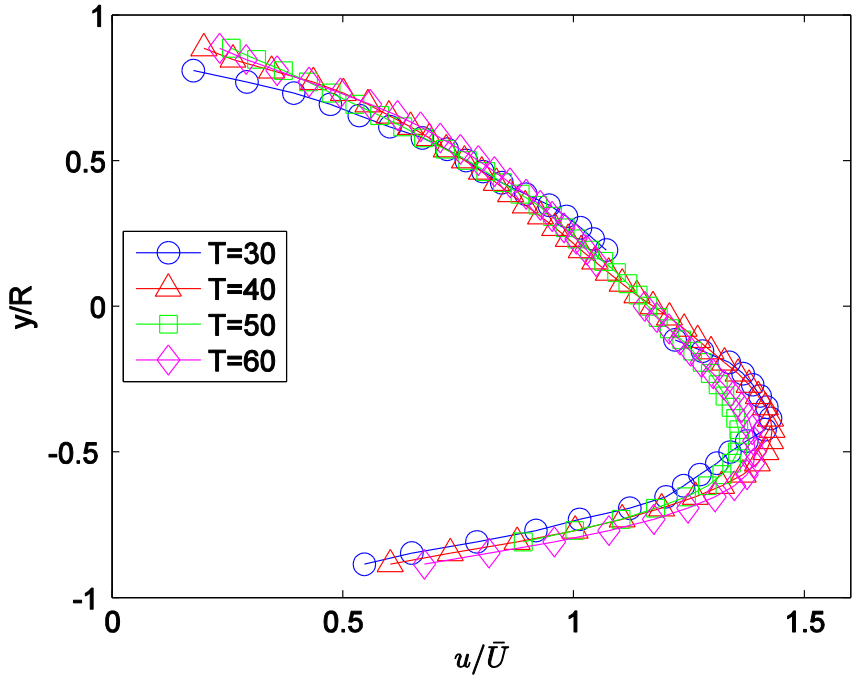
T=30
T=40
T=50
T=60
y/R
$u/\bar{U}$
1
0.5
0
-0.5
-1
0
0.5
1
1.5

B.

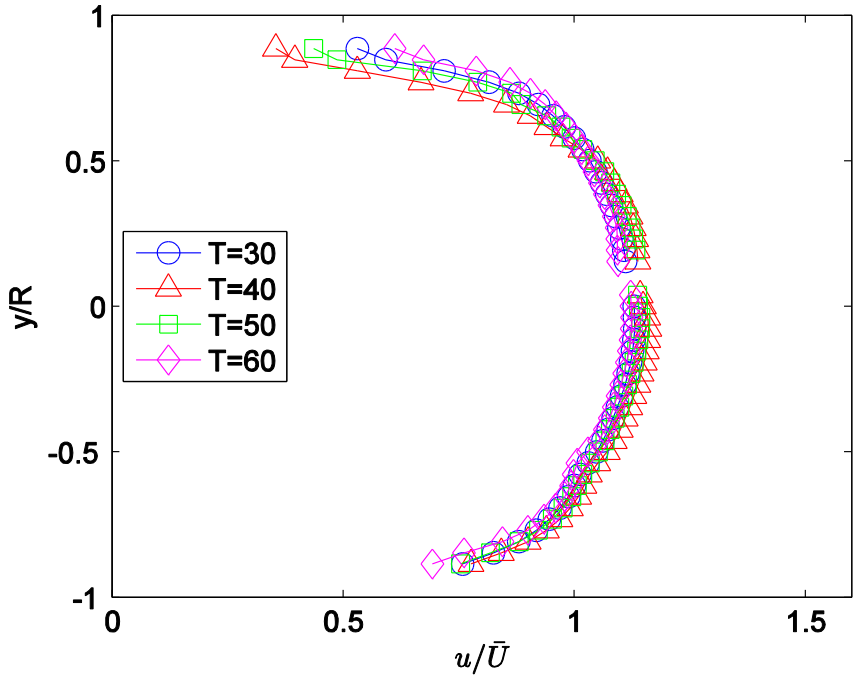

C.

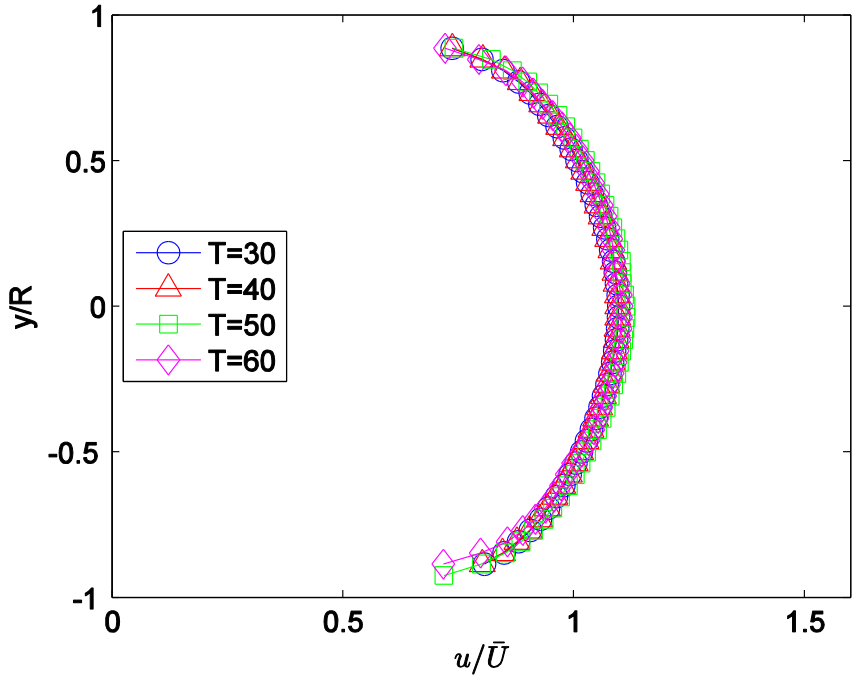

D.

Figure 4.3: Normalized mean streamwise component velocity against the normalized height of the pipe for volumetric flow rates of A) 0.1, B) 0.2, C) 0.6, D) 1 gpm

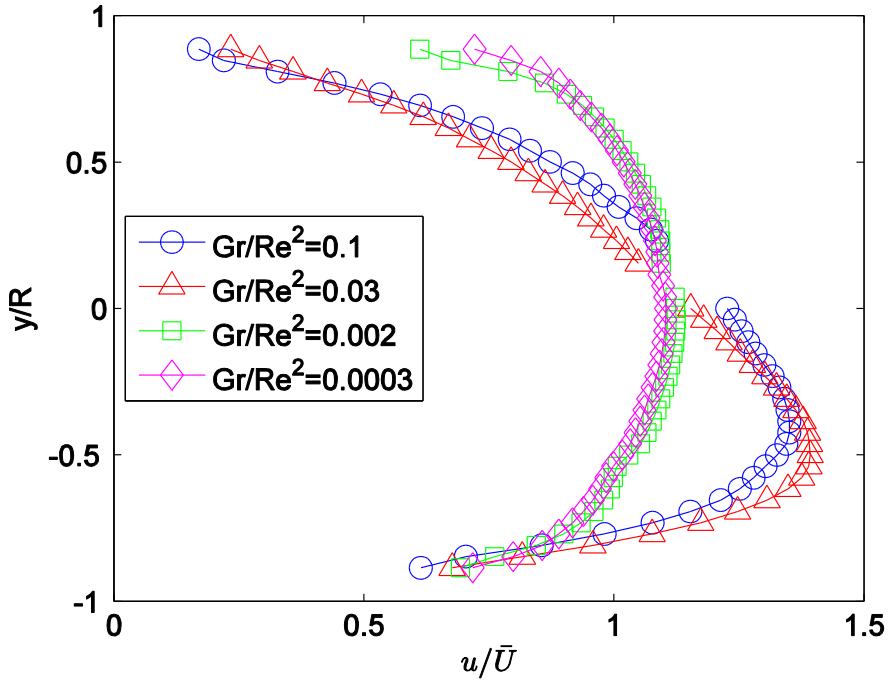

Figure 4.4: Normalized streamwise velocity component against the normalized height of the pipe for interval buoyancy-inertia ratios.

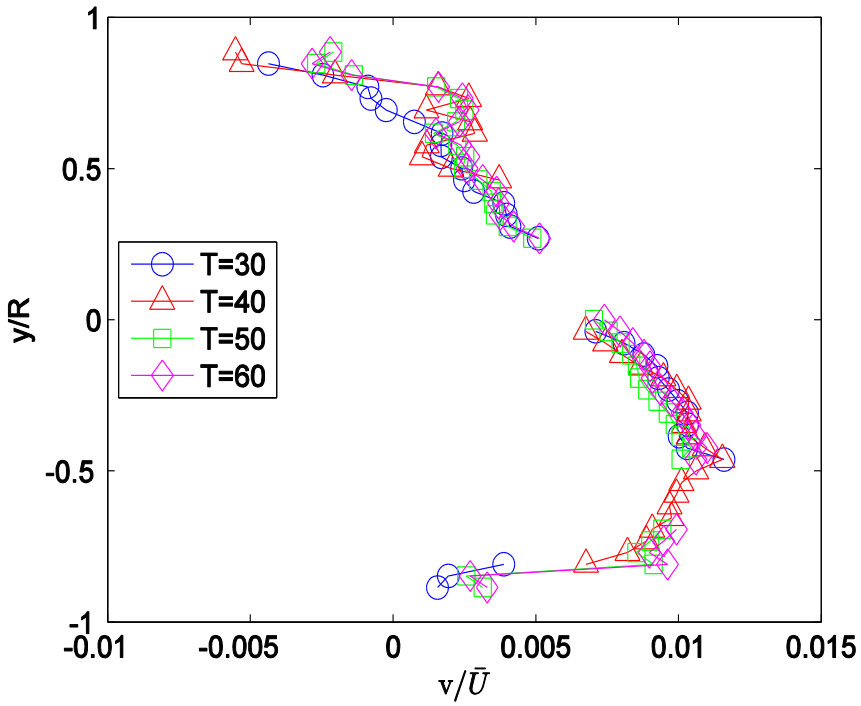

A.

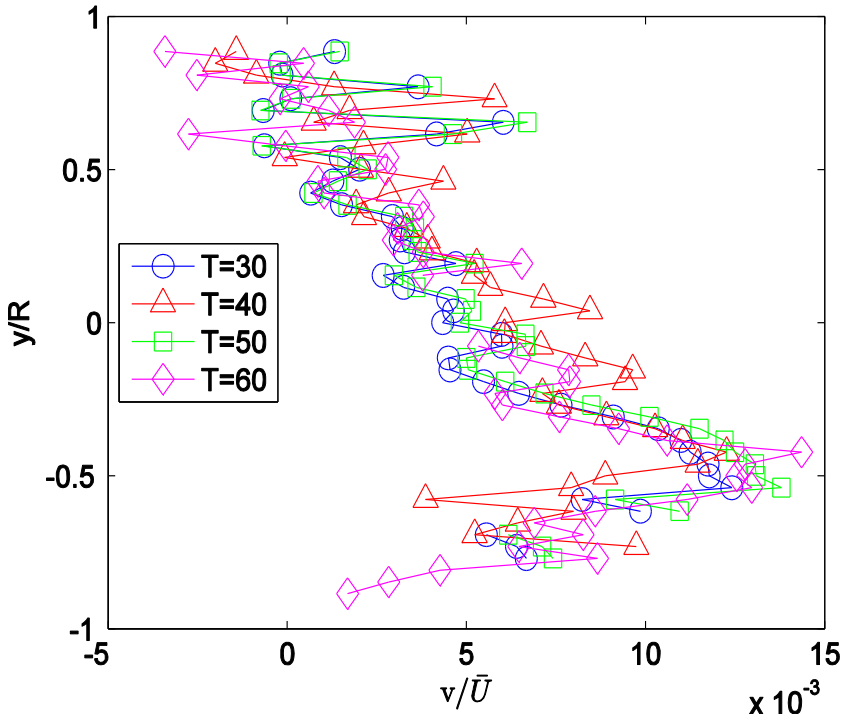

B.

Figure 4.5: Normalized mean vertical velocity component against the normalized height of the pipe for volumetric flow rates of A) 0.1 and B) 0.2 gpm

4.3 RMS Velocity Fields

The mean velocity profile is not sufficient in characterizing a turbulent flow due to the presence of vortices and other turbulent features, as shown in Figure 4.2. The magnitude of turbulent velocity was quantified through root-mean-square (RMS) as follows,

$$u_{RMS} = \sqrt{\frac{1}{N}\sum_{i=0}^{N} u_i^2} \quad (4.2)$$

where u_i is the ith turbulent velocity in the chosen direction and N is the total number of samples. The RMS streamwise and vertical turbulent velocities were computed throughout the height of the tube for each condition. The lowest flow rate that corresponded to the case of $Re = 330$ (at room temperature) was not considered since the turbulent velocity fluctuations even in the presence of heating were almost nonexistent.

The turbulent velocities during convection were normalized by a characteristic velocity scale. For forced convection, friction velocity is generally used as the velocity scale. The friction velocity is given as,

$$u_* = \sqrt{\nu \frac{dU}{dy}\Big|_{y=0}} \quad (4.3)$$

Where ν is the kinematic viscosity and $\frac{dU}{dy}\Big|_{y=0}$ is the mean velocity gradient in the vertical direction at the boundary. Unfortunately, as discussed above, the boundary of this figure was masked due to limitations of the experimental apparatus. To find the gradient in vertical velocity at this location, an approximate extrapolation method was used. From classical turbulent flow theory, a viscous sublayer exists at the boundary in which the mean velocity gradient remains constant (i.e. a constant slope). The friction velocity was computed by assuming the velocity gradient to be constant between the lowest measured point and the wall.

Figures 4.6 and 4.7 illustrate contours of the RMS streamwise and vertical turbulent velocity fields, respectively, in the measurement plane at two values of Gr/Re^2. In Figure 4.6, the results showed that the RMS streamwise turbulent velocity was maximum near the walls and minimal in the center. Note that the RMS velocity should have decreased to zero at the walls, but these areas were masked out and hence the decay of turbulent velocity was not visible in the figure. As the Reynolds number increased i.e. the Gr/Re^2 value decreased (Figure 4.6b), the streamwise turbulent velocity magnitude increased near the wall, as expected, however the overall flow structure and velocity magnitudes remain similar. The results also showed that at a given height, the streamwise turbulent velocity remained almost constant along the tube. Figure 4.7 illustrates the RMS vertical turbulent velocity contours. The results showed that the vertical turbulent velocity was significantly influenced by the Gr/Re^2 values. At Gr/Re^2 = 0.002, the vertical turbulent velocity magnitude was almost zero near the walls, which increased with height but remained fairly constant in most of the pipe domain. As the Gr/Re^2 value decreased due to an increase in the Reynolds number, the overall magnitude of the vertical turbulent velocity increased throughout the pipe domain. The flow structure also changed with the peak velocity magnitudes near the walls, which gradually decreased towards the pipe center. The overall vertical turbulent velocity magnitude at this condition was almost twice that of at Gr/Re^2 = 0.002. The results in Figure 4.7 also showed that at a given height the structure of vertical turbulent velocity remained relatively similar along the pipe at a given value of Gr/Re^2. These results indicated that the overall structure of the turbulent flow was mainly influenced in the direction normal to the pipe wall, which was expected from classical turbulence theory. Comparison of streamwise and vertical turbulent velocity magnitudes in Figures 4.6 and 4.7 showed that the streamwise turbulent velocity magnitudes were higher than the vertical turbulent velocity magnitudes for both cases.

Figure 4.8 illustrates the normalized profiles of the RMS streamwise turbulent velocity versus the normalized height of the pipe at three flow rates. The profiles in Figure 4.8(a) are for the flow rate of $0.2\ gpm$. As discussed earlier, this flow corresponded to the case when the flow was in the transitional regime (Re =1330). The results showed a behavior

similar to that observed in Figure 4.6, i.e. the streamwise turbulent velocity magnitude was largest close to the wall, which then decreased to a minimal value in the core of the pipe. However, the magnitude of turbulent velocity was very low. This result implied that the wall heating introduced buoyancy-induced instabilities in the flow that caused a transition of a laminar flow into turbulence. The results also indicated that these instabilities generated turbulence primarily in the near-wall regions. With an increase in height, the turbulence magnitude rapidly decreased to very small value, confirming that the turbulence was almost negligible in the core region of the pipe. At the two higher flow rates that corresponded to the turbulent regime in the absence of heating (Re = 4000 and 6660), the streamwise turbulent velocity magnitudes were significantly higher although the flow structure remained very similar to that observed in Figure 4.6. The results also showed that at a given flow rate, the wall heating did not have any significant impact on the structure of the streamwise turbulent velocity in the wall-normal direction.

Figure 4.9 shows the profiles of the RMS vertical turbulent velocity versus the normalized height of the pipe corresponding to the same cases shown in Figure 4.8. At the flow rate of $0.2\ gpm$ (Figure 4.9a), as expected, the turbulent velocity magnitude was very low and did not show any trend indicating that the vertical turbulent velocity fluctuations were almost negligible throughout the pipe domain at this flow rate regardless of the bottom wall temperature. The large fluctuations in this profile are due to the relative scale of the axis being comparable to the attributed PIV error scale. As the flow increased to the turbulent regime (Figure 4.9 b & c), the structure of the vertical turbulent velocity was well defined. The results at both of these flow rates show relatively symmetric behavior with peak velocity magnitudes close to the walls. Comparison of the profiles at different heating conditions at a given flow rate, showed that the heating condition did not have an impact on the structure of the vertical turbulent velocity, similar to that of the streamwise turbulent velocity shown earlier.

The RMS streamwise and vertical turbulent velocity profiles at the two higher flow rates in Figures 4.8 and 4.9 show symmetric behavior, which indicated that the turbulence was fully established in the pipe cross-sectional plane. The peak velocity magnitudes near the pipe wall enhanced mixing which increased the transportation of heat from the wall into

the bulk fluid. This resulted in an almost uniform fluid temperature inside the pipe as shown in Figure 3.7 (d & e), and also enhances the heat transfer rate as shown in Figure 3.1. The structure of both streamwise and vertical turbulent velocities were different from that observed in mixed convection at higher Gr/Re^2 values [38] but relatively similar to that observed in the pipe flow in the absence of heating. This confirmed that at low Gr/Re^2 values, the mechanism of turbulence production was primarily the mean shear flow, not the buoyancy. The results further showed that when the contribution of buoyancy-driven flow (natural convection) was smaller than that of the inertia-driven flow (forced convection), i.e. Gr/Re^2 was less than unity, the role of buoyancy was primarily limited to the initiation of instabilities in the laminar flow to trigger the transition to turbulent flow at low Reynolds numbers.

A.

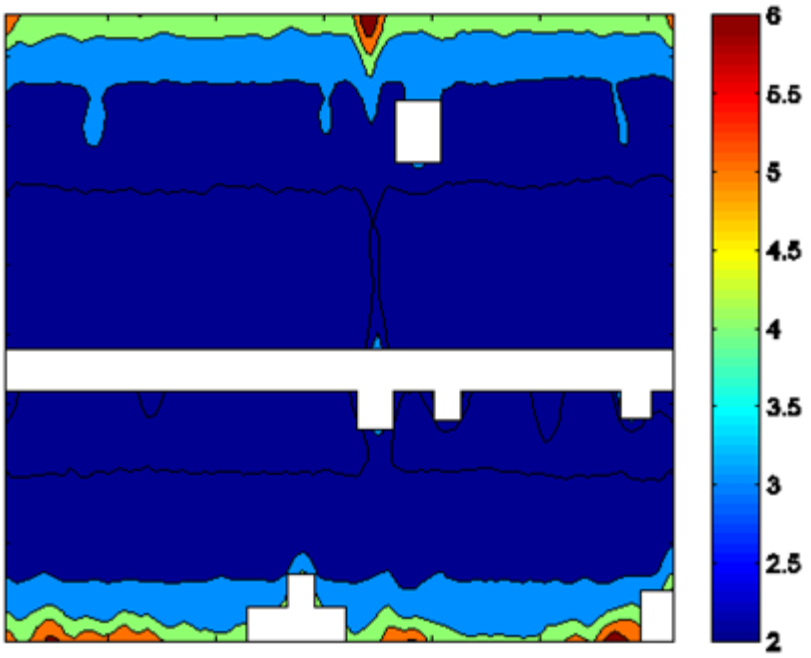

B.

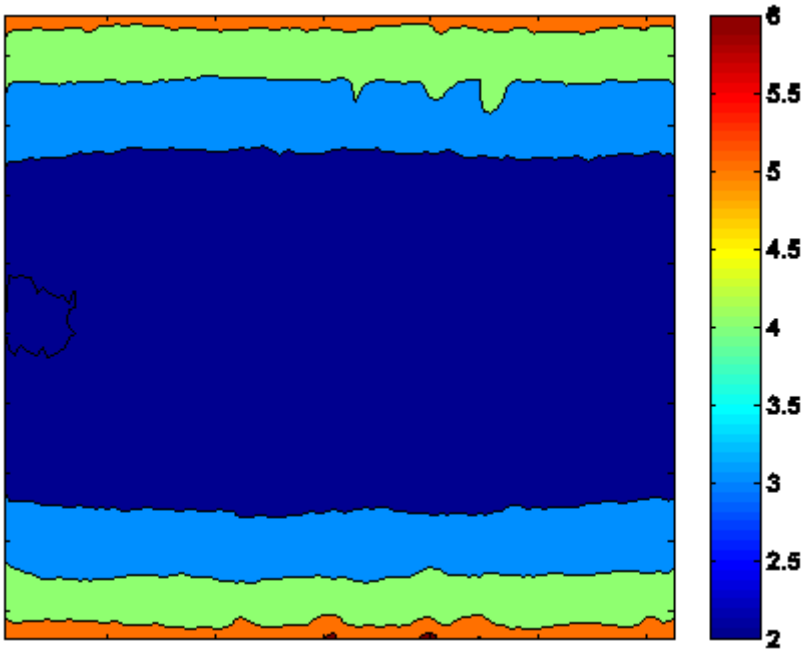

Figure 4.6: Streamwise RMS velocity contour maps for conditions of buoyancy-inertia ratio of A) 0.002, B) 0.0003, with colour bar units of [mm/s]

A.

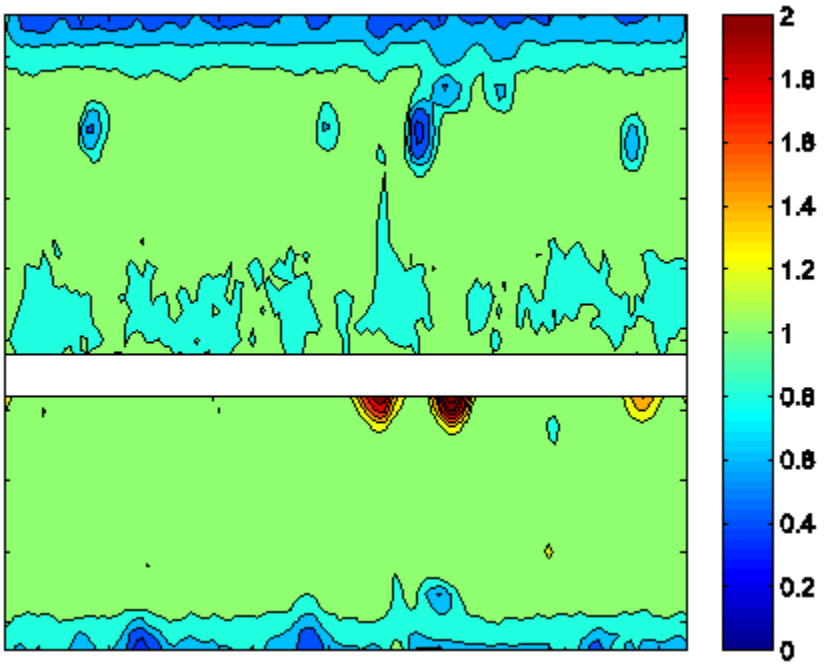

B.

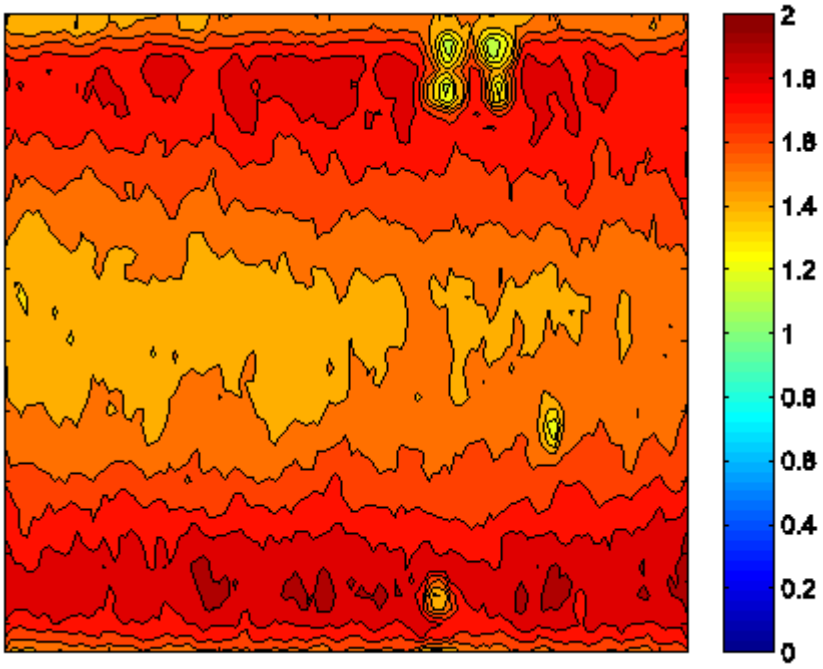

Figure 4.7: Vertical RMS velocity contour maps for conditions of buoyancy-inertia ratio of A) 0.002, and B) 0.0003 with colour bar units of [mm/s]

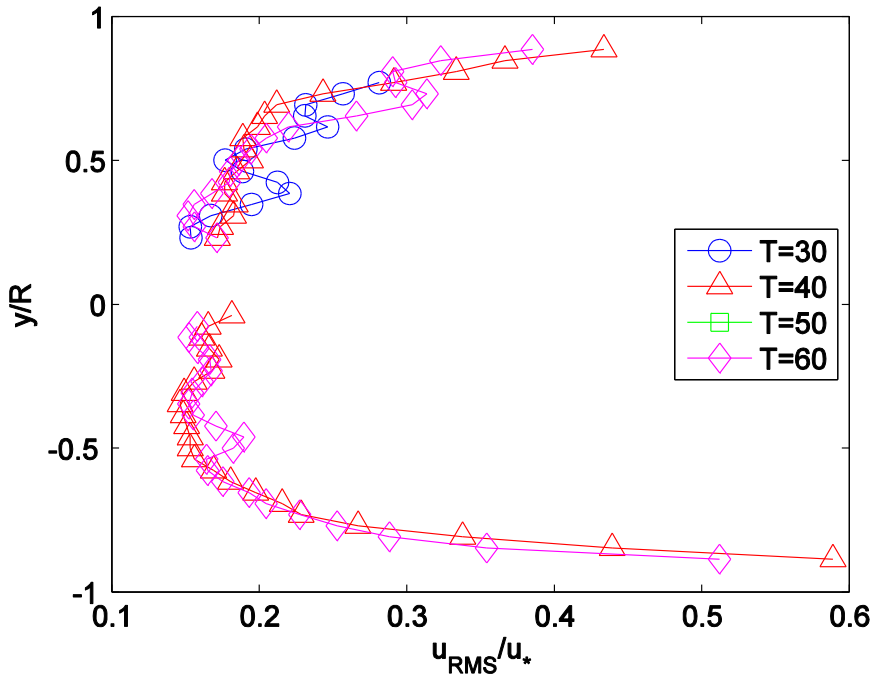
1
0.5
0
-0.5
-1
y/R
0.1
0.2
0.3
0.4
0.5
0.6
u_RMS/u*
T=30
T=40
T=50
T=60

A.

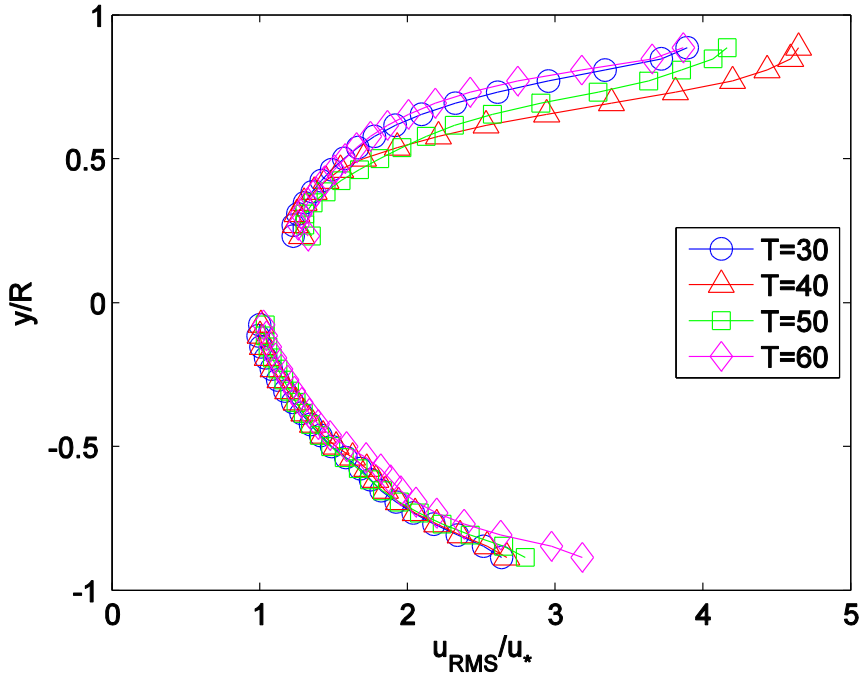
1
0.5
0
-0.5
-1
y/R
0
1
2
3
4
5
u_RMS/u*
T=30
T=40
T=50
T=60

B.

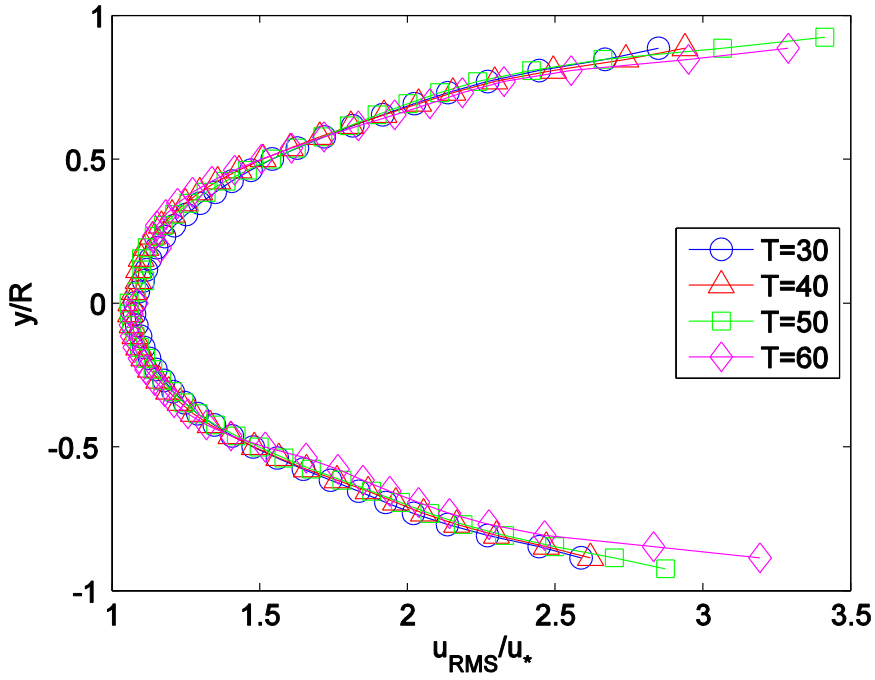

C.

Figure 4.8: Streamwise RMS velocity profile plotted against the normalized height of the pipe for volumetric flow rates of A) 0.2, B) 0.6 and C) 1 gpm

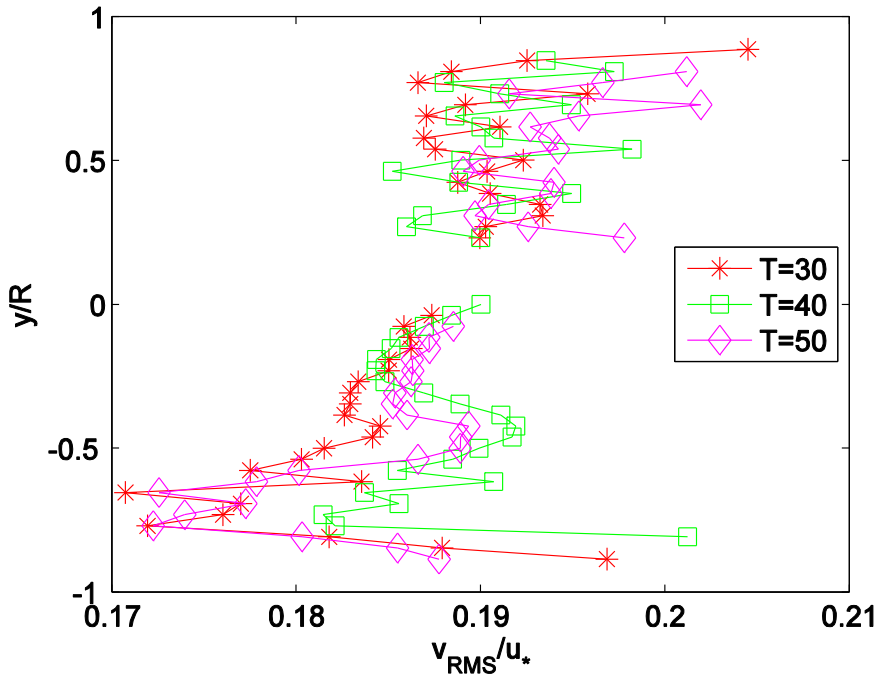
1
0.5
0
-0.5
-1
y/R
0.17
0.18
0.19
0.2
0.21
v_RMS/u*
T=30
T=40
T=50

A.

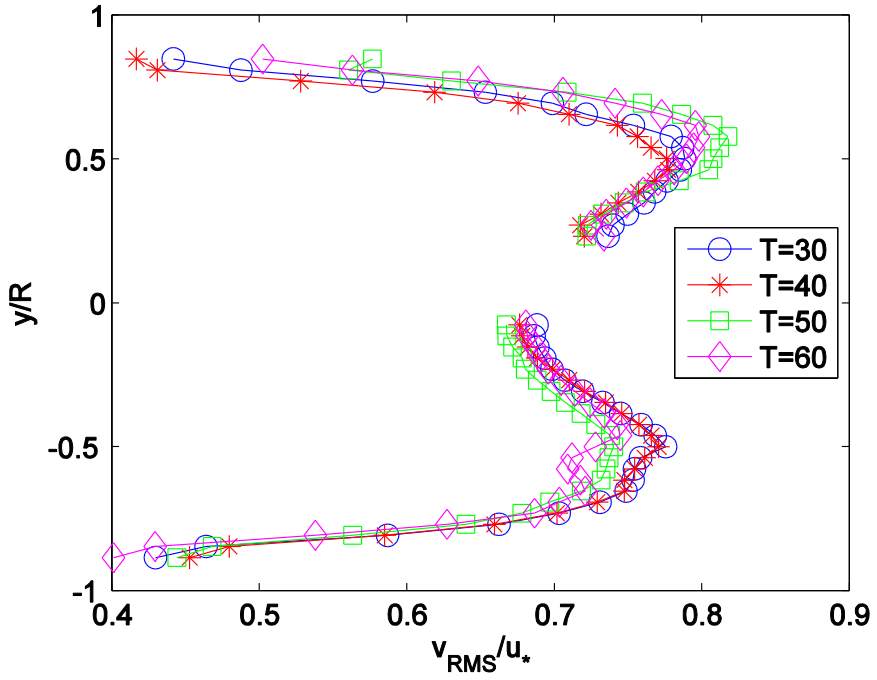
1
0.5
0
-0.5
-1
y/R
0.4
0.5
0.6
0.7
0.8
0.9
v_RMS/u*
T=30
T=40
T=50
T=60

B.

C.

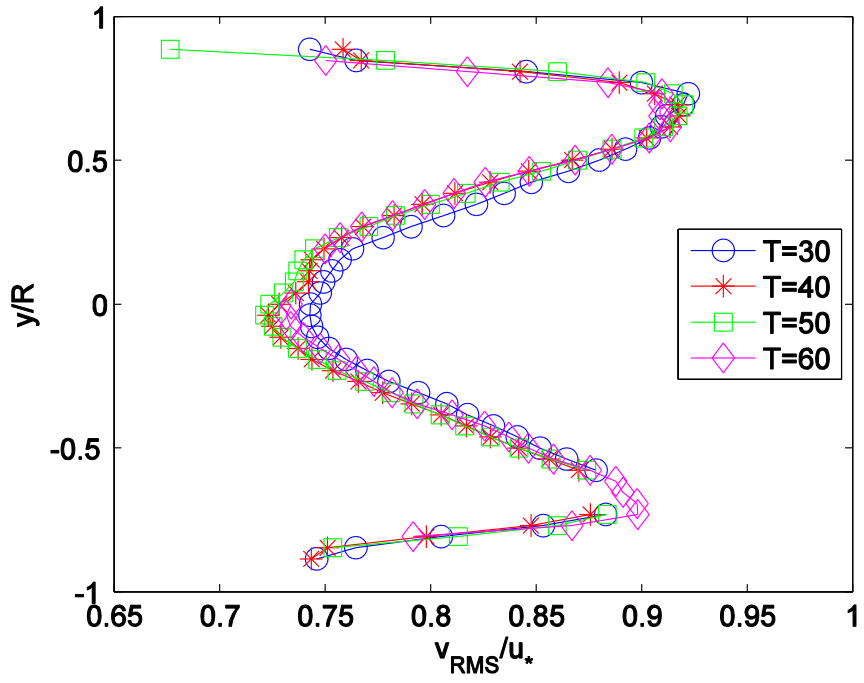

Figure 4.9: Horizontal RMS velocity profile plotted against the normalized height of the pipe for volumetric flow rates of A) 0.2, B) 0.6 and B) 1 gpm

4.4 Conclusions of this Chapter

This chapter focused on the PIV acquired velocity vector fields (positioned in a plane parallel to the direction of flow and normal to the bottom wall). In the previous chapter, it was concluded that a temperature gradient existed inside the pipe due to buoyantly driven momentum transport in the fluid residing in the lower pipe region at low Reynolds numbers and higher Gr/Re^2 values. These conclusions were supported in the present chapter by the acquired wall-normal velocity fields that clearly illustrated a prominent existence of vertical convective currents in the lower region of the pipe. The magnitude of the vertical component of the velocity in the near wall region was much lower than the magnitude of the streamwise velocity component, supporting the low Gr/Re^2 values.

There was a slight trend for the fluid in the top region to have a downwards velocity, which slightly increased in magnitude with decreasing flow rate.

In this chapter, it was also concluded that the present convective behaviour (i.e. the heat transfer into the submerged pipe), effected the mean streamwise velocity structure in the vertical plane of the pipe. Specifically, the temperature gradient forced the mean velocity peak to shift from the middle of the pipe into the lower region. This altered the classical Poiseuille-flow velocity profile and relatively increased the convective heat transfer rates in the lower region of the pipe, indicating larger buoyant forces in this region. The mean velocity profiles recovered their classical trend at high Reynolds numbers where the flow was in fully turbulent regime. The results also show that the mean velocity profiles were approximately independent of the bottom wall temperature, supported by the similar values of Gr/Re^2 for a given flow rate. It was also found that the peaks of the wall-normal and streamwise profiles coincided.

The RMS turbulent velocity fields at the higher Reynolds numbers showed that the streamwise turbulent velocity was maximum near the bottom and minimal in the center. The velocity magnitude increased near the wall with an increase in the Reynolds number, i.e. a decrease in Gr/Re^2. The vertical turbulent velocity was found to be significantly influenced by the Gr/Re^2 values. The vertical turbulent velocity increased throughout the pipe domain as the Gr/Re^2 value decreased due to an increase in the Reynolds number. These results indicated that the overall structure of the turbulent flow was mainly influenced in the direction normal to the pipe wall, which was expected from classical turbulence theory. It was also observed that the streamwise turbulent velocity magnitudes were higher than the vertical turbulent velocity magnitudes for both cases. The results also showed that the magnitudes of both streamwise and vertical turbulent velocities were almost constant along the tube at a given height.

The RMS turbulent velocity profiles showed very low turbulent velocity magnitudes at 0.2 gpm (corresponded to the case when the flow was in the laminar regime in the absence of heating) implying that the wall heating introduced buoyancy-induced instabilities in the flow that caused the transition of a laminar flow into turbulence. At the

two higher flow rates that corresponded to the turbulent regime in the absence of heating, higher velocity magnitudes and almost symmetric behavior were seen, indicating that the turbulence was fully established in pipe's cross-sectional plane. It was concluded that at low Reynolds numbers when the contribution of buoyancy-driven flow (natural convection) was smaller than that of the inertia-driven flow (forced convection), the role of buoyancy was primarily limited to the initiation of instabilities in the laminar flow to trigger the turbulence transition.

Chapter 5

5 Conclusions

An experimental study was conducted to investigate the thermo-fluid behavior in a horizontal pipe fully submerged in a hotter fluid. The temperature and velocity fields were measured to characterize the transport processes over a range of flow and thermal conditions that correspond to a variation in the relative magnitudes of free and forced convection. A thermocouple rake was constructed to acquire temperature measurements at nine internal locations as well as several measurements on the pipe surface and hotter fluid. The PIV technique was employed to measure two-dimensional velocity fields in the mid-vertical plane of the pipe.

5.1 Discussion Summary

All experimental conditions included in this study exhibited a buoyancy-inertia ratio of less than unity, implying the prominent mode of convection preset was forced convection. Although this was the more prominent convective mode, natural convection still existed in comparable quantities at low flow rates and higher wall temperatures. In the laminar flow rate regime, this ratio maintained a range between 0.01 and 0.6. Inside the test setup, the bottom wall heating induced heat transfer into the secondary fluid that resided in the outer reservoir, which in turn induced a heat transfer into the primary fluid through the pipe wall.

The temperature of the outer surface of the pipe was measured, and so was the temperature of the secondary fluid in the outer reservoir. It was determined that the secondary fluid exhibited a uniform temperature in the reservoir domain, while the temperatures around the pipe surface were not uniform. The change in temperature close to the pipe surface was attributed to the heat transfer interaction with the primary fluid. The Gnielinski correlation provided a good theoretical outline for the expected Nusselt numbers. It was found that for the two lowest bottom wall temperature, the resulting Nusselt numbers for different Re and Pr were in close agreement to the theoretical correlation. The Nusselt number was also found to decrease with an increase bottom wall

temperature and Gr/Re^2 in the transitional and turbulent regimes, indicating that turbulent convective heat transfer was damped by an increase in natural convection.

At low Reynolds numbers that correspond to the laminar flow regime in the absence of heating, strong vertical temperature gradients existed inside the pipe cross-sectional plane within primary. This temperature gradient (cooler on the bottom, and hotter at the top) increased in magnitude with an increase in Gr/Re^2. It was also found that the outer pipe surface was hotter on top with respect to the bottom. In addition, the temperature difference between the outer pipe surface temperature and the fluid on the inner pipes surface was largest in the bottom region of the pipe, which indicated a larger heat transfer rate there. The variations in the heat transfer rate were proposed to be present for the following reasons. The unstable stratification in the bottom region of the pipe induced convective motions, which were responsible for the larger heat transfer rate through the bottom of the pipe. In the upper region of the pipe, the stable stratification prevented the convective motions resulting in a significantly low heat transfer rate. This variation in the heat transfer rate in turn influenced the local surface temperature along the pipe periphery. This conclusion was supported by the acquired wall-normal velocity profiles. It was shown that, during initially laminar flow, the vertical velocity magnitude is relatively large in the bottom region of the pipe and almost absent in the op region. There was also a slight trend for the fluid in the top region to have a small downwards velocity that increased in magnitude with a decrease in flow rate.

This wall normal thermal behavior influenced the flow structure resulting in a lower magnitude of streamwise fluid velocity in the upper region compared to that in the bottom region. The streamwise velocity profile was therefore altered from typical Poiseuille flow into an asymmetric profile with a velocity peak shifted towards the bottom wall. This effect even further increased the relative heat transfer rate between the top and bottom fluid regions, increasing the convective heat transfer rate in the bottom region. This was because the fluid parcel at the bottom of the pipe exhibited a larger flux out of the region due to upwards convection.

At high Reynolds numbers that correspond to the fully turbulent regime in the absence of heating, the temperature profiles appeared relatively uniform in comparison. This was expected due to the efficient fluid mixing induced by turbulence. The uniform temperature field in the vertical plane reduced fluid stratification which in turn caused a substantial reduction in the magnitude of local convective motions. The mean and turbulent velocity profiles under these conditions were found to be similar to the classical trend indicating that in the turbulent regime with predominantly forced convection mode, the buoyancy has negligible influence on the mean flow structure.

The results in this study showed that the original flow regime (in the absence of heating) had significant impact on the local temperature field as well as the mean and turbulent flow structure. At low Reynolds numbers that corresponded to an originally laminar flow in the absence of heating, the heat transfer from the outer pipe surface influenced the local flow and temperature behavior that in turn influenced the local heat transfer rate. Whereas, at high Reynolds numbers that corresponded to an originally turbulent flow in the absence of heating, the enhanced fluid mixing caused uniformity in the temperature field and the mean and turbulent flow structure remained unaltered by the buoyancy forces. It is concluded that, at low Reynolds numbers when the contribution of buoyancy-driven flow (natural convection) is smaller than that of the inertia-driven flow (forced convection), the role of buoyancy was primarily limited to the initiation of instabilities in the laminar flow to trigger the transition into turbulence.

5.2 Future Considerations

The present study investigated the thermal and flow behaviours of the fluid at a location where it was fully developed. In real applications, significant heat transfer could occur within the pipe length, in which the flow undergoes a developing phase. Therefore, it is recommended to investigate these behaviours within the developing length inside the pipe to determine the change in heat transfer rate along the pipe and evaluate parameters that influence this transport process. Such investigation should be conducted axially and circumferentially (preferably with a higher resolution than that used in the present study)

due to the non-uniform heating conditions. This would provide a more adaptive insight into the underworking of the heat transfer process along the pipe during hydrodynamic and thermal development of the fluid. It may also provide insight into the origins of the thermal and flow profiles observed in the fully developed region.

Another influential component of the above heat transfer process was the behaviour of the secondary fluid that resided in the external reservoir in the test heat exchanger. Discrete temperature gradients present in the secondary fluid were measured from the surface of the external wall to the surface of the internal pipe. Convective flows must have been present in this reservoir, which influenced the heat transfer in a presently unknown way. For example, secondary fluid natural convection along the side of the pipe would induce a larger convective heat transfer rate into the primary fluid in this side region. These, and similar, behaviours are presently undetermined. These are recommended to be thoroughly investigated using thermocouples and PIV.

While the present study was focused on heat transfer from a hotter surrounding fluid into a submerged pipe, a variety of applications involve heat transfer from the submerged pipe flow into the surrounding fluid. It is expected that the local thermal and fluid behavior in both internal and external fluid would not be similar to that observed in for former case. Hence, it is recommended to conduct a thorough investigation considering the heat transfer in the opposite direction.

References

[1] F. M. White, Viscous fluid flow (3rd ed.), McGraw-Hill (2005) ISBN: 978-007402315.

[2] R. Krishnamurti, On the transition to turbulent convection, J. Fluid Mech. 42 (1970) 295-320.

[3] H. V. Mahaney, F. P. Incropera, S. Ramadhyani, Development of laminar mixed convection flow in a horizontal rectangular duct with uniform bottom heating, Numerical Heat Transfer 12 (1987) 137-155.

[4] D. G. Osborne, F. P. Incropera, Laminar, mixed convection heat transfer for flow between horizontal parallel plates with asymmetric heating, Int. J. Heat Mass Transfer 28 (1985) 207-217.

[5] F. P. Incorpera, J. A. Schutt, Numerical simulation of laminar mixed convection in the entrance region of horizontal rectangular channel, Numerical Heat Transfer 8 (1985) 707-729.

[6] J. R. Maughan, F. P. Incropera, Experiments on mixed convection heat transfer for airflow in a horizontal and inclined channel, Int. J. Heat Mass Transfer 30 (1987) 1307-1318.

[7]D. G. Osborne, F. P. Incropera, Experimental study of mixed convection heat transfer for transitional and turbulent flow between horizontal parallel plates, Int. J. Heat and Mass Transfer 28 (1985) 1337-1344.

[8] S. V. Patil, P. V. Vijay Babu, Experimental studies on mixed convection heat transfer in laminar flow through a plain square duct, Heat Mass Transfer 48 (2012) 2013-2021.

[9] S. T. Gajusingh, M. H. K. Siddiqui, The influence of wall heating on the flow structure in the near-wall region, Int. J. Heat Fluid Flow 29 (2008) 903-915.

[10] C. I. H. Nicholl, Some dynamical effects of heat on a turbulent boundary layer, Journal of Fluid Mech. 40 (1970) 361-384.

[11] S. P. S. Arya, Buoyancy effects in a horizontal flat-plate boundary layer, Journal of Fluid Mech. 68 (1975) 321-343.

[12] K. Rued, J. Y. Murthy, D. E. Metzger, Turbulent convection heat transfer at the corner intersection of heated and unheated walls in a square flow channel, Heat Transfer in Gas Turbine Engines (1987) 49-55.

[13] K. Fukui, M. Nakajima, Unstable stratification effects on turbulent shear flow in the wall region, Int. Journal of Heat and Mas Transfer 28 (1985) 2343-2352.

[14] M. Hirota, H. Fujita, H. Yokosawa, H. Nakai, H. Itoh, Turbulent heat transfer in a square duct, Int. Journal of Heat and Mass Transfer (1997) 170-180.

[15] K. Ichimiya, Y. Yamada, Mixed convection in a horizontal square duct with local inner heating, Heat Transfer-Asian Research 34 (2005) 160-170.

[16] A. E. Perry, P. H. Hoffman, An experimental study of turbulent convective heat transfer from a flat plate, Journal of Fluid Mech. 77 (1976) 355-368.

[17] L. W. Wang, K. H. Hou, I. G. Lu, C. F. Hsu, Flow patterns of mixed convection in a horizontal square channel flow, Exp. Heat Transfer 9 (1996) 257-265.

[18] W. L. Lin, T. F. Lin, Experimental study of unstable mixed convection of air in a bottom heated horizontal rectangular duct, Int. J. Heat Mass Transfer 39 (1996) 1649-1663.

[19] K. Nandakumar, J. H. Masliyah, H. Law, Bifurcation in steady laminar mixed convection flow in horizontal ducts, J. Fluid Mech. 152 (1985) 145-161.

[20] C. C. Huang, T. F. Lin, Buoyancy induced flow transition in mixed convection flow of air through a bottom heating horizontal rectangular duct, Int. J. Heat Mass Transfer 37 (1994) 1235-1255.

[21] S. Sookdeo, K. Siddiqui, Investigation of the flow field inside flat-plate collector tube using PIV technique, Solar Energy 84 (2012) 917-927

[22] A. Elatar, S. Siddiqui, The effect of mixed convection on the structure of channel flow at low Reynolds numbers, Int. Journal of Heat and Fluid Flow 46 (2014) 29-42.

[23] A. Elatar, Siddiqui, The influence of bottom wall heating on the mean and turbulent flow behaviour in the near wall region during mixed convection, Int. Journal of Thermal Sci. 77 (2014) 233-243.

[24] F. M. White, Fluid Mechanics. McGraw-Hill (2003). ISBN 0-07-240217-2.

[25] W. H. Snyder, J. L. Lumley, Some measurements of particle velocity autocorrelation functions in a turbulent flow, J. Fluid Mech. 48 (1971) 41-71.

[26] D. A. Siegel, A. J. Plueddemann, The motion of a solid sphere in an oscillating flow; an evaluation of remotely sensed Doppler velocity estimates in the sea, J. Atmos. Oceanic Tech. 8 (1991) 296-304.

[27] S. B. Pope, Turbulent Flows, Cambridge University Press, 2000.

[28] P. K. Kundu, I. M. Cohen, Fluids Mechanics (2^{nd} ed.), 2002.

[29] H. Tennekes, J. L. Lumly, A first course in turbulence, MIT Press, Cambridge, 1972.

[30] F. Veron, W. K. Melville, Pulse-to-Pulse coherent Doppler measurements of waves and turbulence, J. Atmos Oceanic Tech. 16 (1999) 1580-1597.

[31] M. H. Jobehdar, K. Siddiqui, A. H. Gadallah, W. A. Chishty, Effect of single- and multi-hole bubble breakers on the effervescent atomization process, Atomization and Sprays 25 (2015) 1-28.

[32] M. H. K. Siddiqui, M. R. Leowen, C. Richardson, W. E. Asher, A. T. Jessup, Simultaneous particle image velocimetry and infrared imagery of micro-scale breaking waves, Phys. Fluids 13 (2001) 1891-1903.

[33] E. A. Cowen, S. G. Monismith, A hybrid digital particle tracking velocimetry technique, Exp. Fluids 22, (1997) 199-211.

[34] A. K. Prasad, R. J. Adrian, C. C. Landreth, P. W. Offutt, Effects of resolution on the speed and accuracy of particle image velocimetry interrogation, Exp. Fluids 13 (1992) 105-116.

[35] F. P Incropera, D. P. Dewitt, Fundamentals of heat and mass transfer (6^{th} ed.), John Wiley & Sons, (2007) ISBN 978-0-471-45728-2.

[36] S. J. K. Bukhari, K. Siddiqui, Turbulent structure beneath air-water interface during natural convection, Physics of Fluids 18 (2006) 0.35106.

[37] R. J. Volino, G. B. Smith, Use of simultaneous IR temperature measurements and DPIV to investigate thermal plumes in a thick layer cooled from above, Experiments in Fluids 27 (1999) 70-78.

[38] A. Elatar, K. Siddiqui, The effect of mixed convection on the structure of channel flow at low Reynolds numbers, Int. Journal of Heat and Mass Transfer 46 (2014) 29-42.

[39] M. Ouzzane, N. Galanis, Numerical analyses of mixed convection inside inclined tubes with external longitudinal fins, Solar Energy 71 (2001) 199-211.

[40] G. Sandhu, K. Siddiqui, Investigation of the fluid temperature field inside a flat-plate solar collector, Heat and Mass Transfer 50 (2014) 1499-1514.

[41] M. Raffel, C. Willert, J. Kompenhans, Particle Image Velocimetry, a practicel guide, (3^{rd} ed.) Springer-Brlein (1998).

Curriculum Vitae

Benjamin Steen Email: ben.s.steen@gmail.com

Post-secondary Education and Degrees:
(B.H.Sc.). 2008-2013
Western University
London, Ontario, Canada

(M.E.Sc.) 2013-2015
Western University
London, Ontario, Canada

Honours and Awards:
Western Graduate Research Scholarship

Related Work Experience:
Teaching Assistant
Western University
2014-2015